PREPARATION OF BORON-ZIRCONIUM CO-DOPED PHOTOCATALYTIC TITANIUM DIOXIDE POWDER

A THESIS SUBMITTED TO
THE GRADUATE SCHOOL OF NATURAL AND APPLIED SCIENCES
OF
MIDDLE EAST TECHNICAL UNIVERSITY

BY
TOLGA TOKMAKCİ

IN PARTIAL FULFILLMENT OF THE REQUIREMENTS
FOR
THE DEGREE OF MASTER OF SCIENCE
IN
METALLURGICAL AND MATERIALS ENGINEERING

JANUARY 2013

Approval of the thesis:

PREPARATION OF BORON-ZIRCONIUM CO-DOPED PHOTOCATALYTIC TITANIUM DIOXIDE POWDER

submitted by **TOLGA TOKMAKCİ** in partial fulfilment of the requirements for the degree of **Master of Science in Metallurgical and Materials Engineering Department, Middle East Technical University** by,

Prof. Dr. Canan Özgen _____
Dean, Graduate School of **Natural and Applied Sciences**

Prof. Dr. Cemil Hakan Gür _____
Head of Department, **Metallurgical and Materials Engineering**

Prof. Dr. Abdullah Öztürk _____
Supervisor, **Metallurgical and Materials Eng. Dept., METU**

Assist. Prof. Dr. Jongee Park _____
Co-Supervisor, **Metallurgical and Materials Eng. Dept., Atılım University**

Examining Committee Members:

Prof. Dr. Muharrem Timuçin _____
Metallurgical and Materials Engineering Dept., METU

Prof. Dr. Abdullah Öztürk _____
Metallurgical and Materials Engineering Dept., METU

Assoc. Prof. Dr. Caner Durucan _____
Metallurgical and Materials Engineering Dept., METU

Assist. Prof. Dr. Y. Eren Kalay _____
Metallurgical and Materials Engineering Dept., METU

Assist. Prof. Dr. Hilal Türkoğlu Şaşmazel _____
Metallurgical and Materials Engineering Dept., Atılım University

Date: *31.01.2013*

I hereby declare that all information in this document has been obtained and presented in accordance with academic rules and ethical conduct. I also declare that, as required by these rules and conduct, I have fully cited and referenced all material and results that are not original to this work.

Name, Last name : Tolga Tokmakci

Signature :

ABSTRACT

PREPARATION OF BORON-ZIRCONIUM CO-DOPED PHOTOCATALYTIC TITANIUM DIOXIDE POWDER

TOKMAKCİ, Tolga

M.Sc., Department of Metallurgical and Materials Engineering

Supervisor: Prof. Dr. Abdullah ÖZTÜRK

Co-Supervisor: Assist. Prof. Dr. Jongee PARK

January 2013, 6Ш pages

A titanium dioxide powder co-doped with boron and zirconium was prepared by mechanical ball milling. Photocatalytic performance of the powder was evaluated by degradation of methylene blue (MB) solution under UV illumination. XRD patterns were refined by Rietveld analysis method to obtain accurate lattice parameters and position of the atoms in the crystal structure of TiO_2. XRD analysis indicated that the B and/or Zr doped TiO_2 powders composed of anatase and did not exhibit any additional phase. Rietveld analysis suggested that dopant B and Zr elements were successfully weaved into crystal structure and distorted the lattice of TiO_2. The highest distortion was obtained by co-doping. SEM investigations confirmed that mechanical ball milling technique led to a decrease in particle size of TiO_2 powder. XPS analysis revealed that dopant B and Zr atoms did not appear in any form of compound including Ti and O elements. Results of photocatalytic activity test suggested that boron and zirconium co-doped TiO_2 particles exhibited a better visible light response and photocatalytic activity than that of mono element doped TiO_2 (i.e. B-TiO_2 and Zr-TiO_2) and undoped TiO_2 particles. A 20% improvement in photocatalytic activity of reference TiO_2 powder (powder ball milled without dopant addition) was achieved by B and Zr co-doping. The enhanced photocatalytic activity is attributed to synergistic effects of B-Zr co-doping the lattice of TiO_2 as well as particle size reduction.

Keywords: photocatalysis; titanium dioxide; boron; zirconium; co-doping; ball milling; methylene blue solution.

ÖZ

BOR VE ZİRKONYUM EŞ- KATKILANMIŞ FOTOKATALİTİK TİTANYUM DİOKSİT TOZUNUN HAZIRLANMASI

TOKMAKCİ, Tolga

Yüksek Lisans, Metalurji ve Malzeme Mühendisliği Bölümü

Tez Yöneticisi: Prof. Dr. Abdullah ÖZTÜRK

Ortak Tez Yöneticisi: Assist. Prof. Dr. Jongee PARK

Ocak 2013, 6Ⅲ sayfa

Mekanik bilyalı öğütme yöntemi ile bor ve zirkonyum eş katkılanmış fotokatalitik titanyum dioksit tozu hazırlanmıştır. Tozun fotokatalitik performansı metilen mavisi (MB) çözeltisinin ultraviyole ışık altında bozunumuna bağlı olarak belirlenmiştir. X-Ray kırılınım analizinden elde edilen desenler, titanyum oksitin latis parametrelerinin ve kristal yapısı içerisindeki atom pozisyonlarının daha hassas elde edilebilmesi için, Rietveld analizi yöntemiyle irdelenmiştir. XRD analizi sonuçları hazırlanan bor ve/veya zirkonyum katkılı tozların anataz olduğunu ve başka hiç bir farklı fazı içermediğini göstermiştir. Rietveld analizi yöntemiyle mekanik bilyalı öğütme tekniği ile katkılanan elementlerin titanyum dioksitin kristal yapısına girdiği ve yapıda çeşitli tahribatlar oluşturduğu kanıtlanmıştır. En büyük tahribatın eş katkılanmış tozlarda oluştuğu belirlenmiştir. SEM fotoğraflarından mekanik bilyalı öğütme tekniğinin titanyum dioksitin ortalama tanecik boyutunda ciddi bir azalmaya neden olduğu onaylanmıştır. XPS analizi katkılanan bor ve zirkonyum atomlarının titanyum ve oksijen içeren herhangi bir bileşik halinde bulunmadığını göstermiştir. Fotokatalitik aktivite test sonuçlarından eş katkılanmış titanyum dioksit tozlarının, katkılanmamış ya da sadece bor veya sadece zirkonyum katkılanmış titanyum oksit tozlarına gore daha yüksek bir fotokatalitik aktivite gösterdiği anlaşılmıştır. Referans titanyum dioksit tozun (dopant ilave edilmeden öğütülmüş toz) fotokatalitik performansı B ve Zr eş-katkılanmasıyla % 20 daha fazla arttırılmıştır. Fotokatalitik aktivitedeki artış, ortalama tanecik boyutundaki düşme ile bor ve zirkonyum eş katkılamasının birlikte etkilerine atfedilmiştir.

Anahtar Kelimeler: fotokataliz; titanyum dioksit; bor; zirkonyum; eş katkılama; mekanik bilyalı öğütme; metilen mavisi solüsyonu

To my family

ACKNOWLEDGEMENTS

I would like to express my deepest gratitude to my advisor Prof. Dr. Abdullah Öztürk for his endless support, guidance and patience throughout the whole time I have worked on this thesis study. Without him, this thesis would not be done.

I would also like to thank Assist. Prof. Dr. Jongee Park for his guidance and expertise throughout all the experimental studies.

I wish to give my special thanks to Assist. Prof. Dr. Yunus Eren Kalay for his very kind support and understanding.

I would like to thank my lab-mates in Photocatalytic Materials Laboratory, whom I feel so lucky to know, Başak Aysin, Esra Çorapçı, Derya Kapusuz, and Lütfi Ağartan for their infinite support and their friendship since the day I have met each one of them. I sincerely thank Anıl Kantarcıoğlu, whom I owe so much, beginning from the first day of my study for being such a valuable, talented and entertaining friend. Lastly, Elif Selen Ateş, Tuba Demirtaş, Şeyda Küçükyıldız, Ayşe Merve Genç, Önder Ulusoy, Gökay Toprak, Emre Gültürk, and Murat Yücel whom I shall not even need to thank since I will surely be seeing them for the rest of my life. I appreciate all the people that I have known in Metallurgical and Materials Engineering Department, METU for the contributions that they have made in the last eight years of my life. I want to acknowledge all the facilities and valuable personnel in this department. I also would like to acknowledge METU Central Laboratory for their kind help with my experiments.

I would like to acknowledge TUBİTAK for the scholarship I received in the last year of my graduate study.

Finally, I would like to thank my parents Aynur and Arif, my brother Yusuf, my sister-in-law Esra, and my lovely niece Cansu for their patience, never ending love and all the other things they have sacrificed in the twenty years of my education. Thank you for always being there for me.

TABLE OF CONTENTS

LIST OF TABLES

TABLES

LIST OF FIGURES

FIGURES

CHAPTER 1

INTRODUCTION

Nowadays, environmental pollution is one of the important issues and has negative outcomes in human lives. Pollutants emitted from various sources result in severe ecological problems such as pollution of air, water or soil (Chatterjee and Dasgupta, 2005). In this regard, semiconductor photocatalysis seems to be more effective than the conventional chemical oxidation methods for decomposition of toxic wastes to non-hazardous products (Legrini et al., 1993). Of the many semiconductor photocatalysts, TiO_2 has been the most widely used and studied one in many applications due to its strong oxidizing capabilities for degradation of organic pollutants, chemical stability, nontoxicity, high durability, ease of availability and low cost (Nakata and Fujishima, 2012; Stamate and Lazar, 2007).

Superior features of TiO_2 photocatalyst such as high oxidizing power and hydrophillicity are made its products commercially usable in the market worldwide (Nakata et al., 2012). Some of the major applications of TiO_2 photocatalysts including environmental and energy related fields are shown in Figure 1.1.

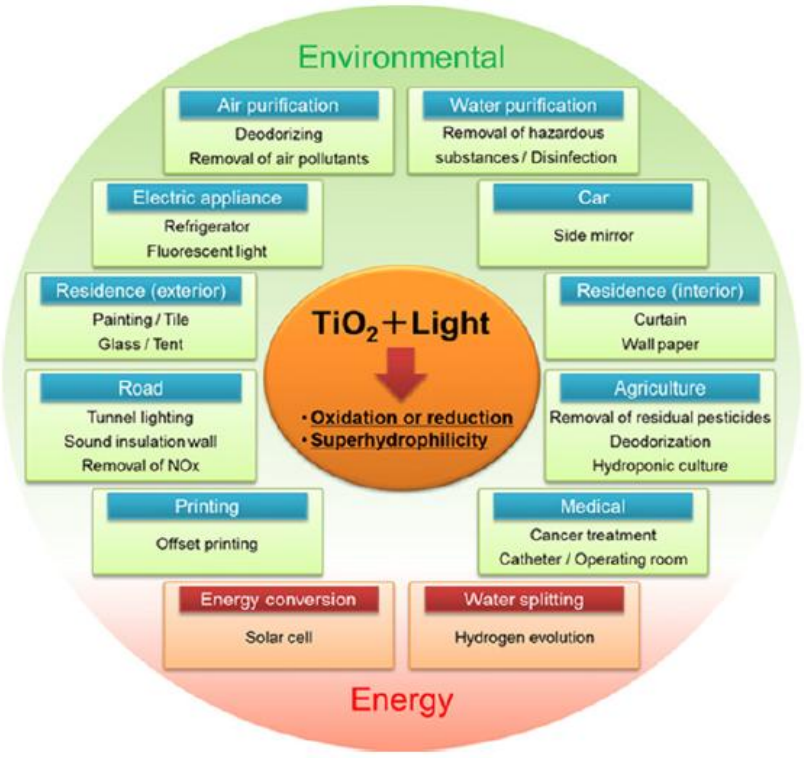

Figure 1.1. Major applications of TiO_2 photocatalyst (Nakata and Fujishima, 2012).

In spite of good peculiarities, high band gap energy (e.i. 3.2 eV for anatase), low photoquantum energy, and high recombination of electron-hole pairs restrict the application of TiO_2 photocatalyst (Zhang and Liu, 2008). A large number of investigations have been carried out to improve photocatalytic efficiency of TiO_2 since TiO_2 photocatalysts show relatively low activity in solar irradiation due to the fact that it is a wide band gap photocatalyst (Li et al., 2006). Therefore, the modification to TiO_2 received great attention and some strategies have been developed to decrease the band gap energy and hence to increase the photocatalytic activity of TiO_2. In order to improve the visible light response and photocatalytic activity of TiO_2, many attempts including doping of TiO_2 with a foreign metal/nonmetal element, sensitizing with an organic dye, and coupling with a narrow semiconductor have been made. Among which, the simplest and most feasible approach seemed to be doping or co-doping of TiO_2 with foreign metal/nonmetal elements. That is, doping or co-doping a metal/nonmetal or a metal and a nonmetal into the lattice of TiO_2. It has been reported that doping or co-doping foreign metal/nonmetal elements into the lattice narrows the band gap of TiO_2, and restricts the recombination of electron-hole pairs thereby improves the visible light photocatalytic activity.

Loading a noble metal like platinum (Pt) (Ishibai et al., 2007), and silver (Ag) (Sobana et al., 2006), doping with a metal like iron (Fe) (Zhu et al, 2004), copper (Cu) (Colon et al., 2006), and zirconium (Zr) (Venkatachalam et al., 2007), doping with nonmetal such as carbon (C) (Kang et al., 2008), sulphur (S) (Ohno et al., 2004), phosphor (P) (Lin et al., 2007), and boron (B) (Chen et al., 2006), compounding TiO_2 with other materials like silica (SiO_2) (Jung et al., 2004), or co-doping a metal and nonmetal atoms like nitrogen (N)-nickel (Ni) (Zhang and Liu, 2008) and B-Fe (Khan et al., 2008) have been studied.

Different chemical production routes such as sol-gel processing, hydrothermal processing and a mechanical route of ball milling have been tried to doping or co-doping of TiO_2 with foreign metal/nonmetal elements. Mechanical ball milling is the simplest and most economical technique among the routes for the production of TiO_2 powders. Although there are some publications on the preparation of B and Zr co-doped photocatalyst TiO_2 through sol-gel (Ling et al., 2008; Yao et al., 2011) and hydrothermal (Liu et al., 2011) production techniques, B and Zr co-doping on TiO_2 particles by mechanical ball milling has not been the subject of any scientific study till now.

The purpose of this study was to improve the visible light response and photocatalytic performance of TiO_2 through co-doping with B and Zr by mechanical ball milling. B was taken as dopant since it has small ionic size (0.23 Å) thus, it could easily incorporate into the lattice structure of TiO_2 and decrease the band gap (Zhang and Liu, 2008). Large ionic size (0.84 Å) of Zr was chosen as a co-dopant metal due to its capability to suppress recombination of electron-hole pairs at the surface of the photocatalyst (Gao et al., 2010). A conventional type of ball mill was employed for preparing B-Zr co-doped nanosize TiO_2 particles since it is relatively cheap and highly versatile. The powders prepared were characterized through X-Ray powder diffraction (XRD), Scanning Electron Microscope (SEM), Energy Dispersive Spectroscopy (EDS), and X-ray Photoelectron Spectroscopy (XPS) analyses. Photocatalytic performances of the powders were evaluated by degradation of methylene blue (MB) under ultraviolet (UV) illumination.

CHAPTER 2

LITERATURE REVIEW

2.1 PHOTOCATALYSIS

Industrialized nations face numerous environmental problems including elimination of hazardous components from contaminated ground waters, soil or air. In order to overcome these problems, advanced physiochemical processes such as semiconductor photocatalysis have been introduced (Hoffmann et al., 1995). Starting in the late 1960s, story began with photoelectrochemical solar energy conversion and then shifted into the area of environmental photocatalysis such as self-cleaning surfaces, water or air purification (Fujishima et al., 2000). The term "photocatalysis" is not meant to imply catalysis by light, since light is acting as a reactant during chemical reaction but rather defined as photoactivated reaction by the presence of a catalyst (Mills and Hunte, 1997). This photon assisted catalytically active species named "photocatalysts", are mostly semiconductor materials which are agreed to be more effective reactants than conventional chemical oxidizers for decomposition of organic wastes to non-hazardous products (Chatterjee and Dasgupta, 2005).

Initial process for photocatalysis reaction is formation of electron (e^-) and hole (h^+) pairs which need photon energy (hv) to overcome band gap energy (E_g) between valance band (VB) and conduction band (CB) of semiconductor (Zhao and Yang, 2003). When E_g is greater than hv, charge will transfer between generated e^- and h^+ pairs and reactants on semiconductor surface and photo-oxidation reaction happens only if redox potentials of e^- and h^+ are suitable for generating redox processes (Chatterjee and Dasgupta, 2005). Thus, probability and rate of charge transfer directly related with redox potentials of adsorbate species and respective positions of band edges of VB and CB (Linsebigler et al., 1995). Also, excited state e^- and h^+ can recombine by dissipating the stored energy as heat within a few nanoseconds without participating in redox reactions at the interface (Hoffmann et al., 1995). A schematic illustration of main processes occurring on semiconductor particle is shown in Figure 2.1.

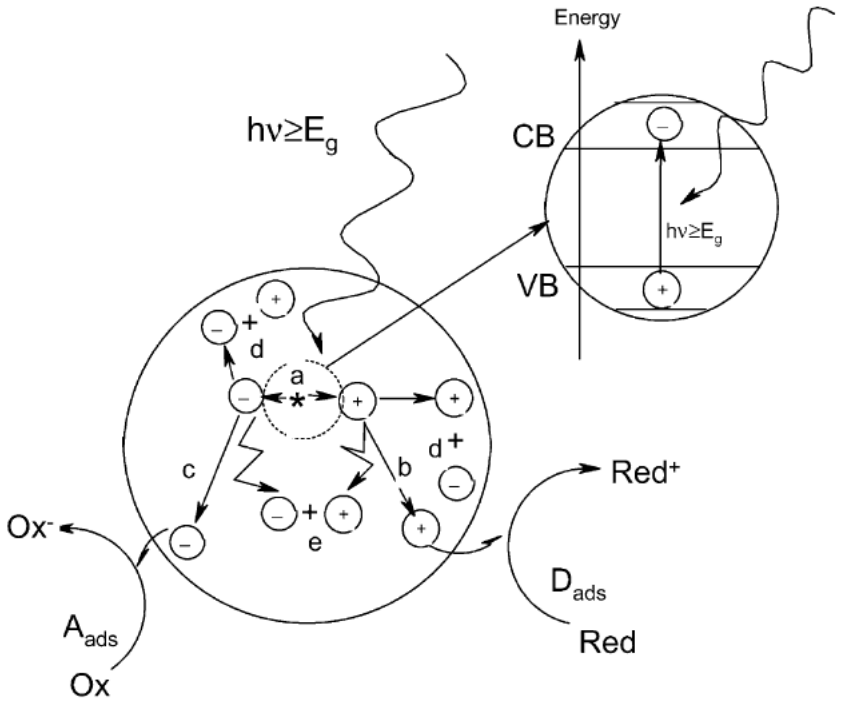

Figure 2.1. Photoexcitation followed by deactivation events in a semiconductor particle (Carp et al., 2004).

After photoexcitation (a), generated of e^- and h^+ pairs can migrate to semiconductor surface where surface hole oxidizes donor species (b) and electron reduces the acceptor (c). The e^- and h^+ recombination is in competition with charge transfer of adsorbed species which can occur on the surface (d) or in the volume (e) of semiconductor particle (Carp et al., 2004). If semiconductor remains intact while charge transfer is continuous and exothermic, the process is called heterogeneous photocatalysis (Linsebigler et al., 1995). The overall heterogeneous photocatalysis reaction can be represented by following equation (Mills and Hunte, 1997);

$$A + D \xrightarrow[h\nu \geq E_g]{\text{Semiconductor}} A^- + D^+ \qquad (\Delta G^\circ < 0)$$

where A and D are acceptor and donor, respectively.

Wide variety of organic contaminants can be pohotodegrated by strong oxidizing power of h^+. However, reducible species must be provided to prevent a charge buildup. Therefore, both oxidative and reductive paths are required in an effective semiconductor photocatalysis. Final products of the reaction are carbon dioxide (CO_2), water (H_2O), and inorganic acids or salts in most of the cases (Hoffmann et al., 1995).

Several semiconductor materials are used for photocatalytic applications. Some of the commonly used semiconductor materials and their band gap values are given in Table 2.1.

Table 2.1. Commonly used semiconductors for photocatalytic applications and their band gap values (Ersöz, 2009; Hernandez-Alonso et al., 2009; Zhao and Yang, 2003).

Semiconductor	**Band Gap (eV)**
TiO_2 (Anatase)	3.2
TiO_2 (Rutile)	3.0
SnO_2	3.6
ZnO	3.4
ZnS	3.7
Fe_2O_3	2.3
CeO_2	3.0
Ga_2O_3	4.6
WO_3	2.8
CdS	2.3
$SrTiO_3$	3.2

For environmental applications, a good photocatalyst must be photoactive, able to utilize visible or near-ultraviolet (UV) light, biologically and chemically inert, photostable and inexpensive. Photocatalyst anatase TiO_2 satisfies all of the criteria above (Mills and Hunte, 1997). Therefore it has been the most extensively studied and most commonly used material for the degradation of harmful organic species. However, due to its large energy band gap (e.i. 3.2 eV for anatase), TiO_2 photocatalysis reaction occurs only under UV-light (λ < 388 nm) irradiation which accounts for only a small fraction (~5%) of the solar spectrum. The large band gap energy severely limits the applications of TiO_2 as photocatalyst (Cheng et al., 2012). Metal sulphide photocatalysts are not desirable due to formation of photoanodic corrosion while the iron oxide semiconductors are not eligible for photocatalytic applications because of photocathodic corrosion. Also, ZnO seems to be an alternative to TiO_2. However $Zn(OH)_2$ yielding on the surface of ZnO particles leads to inactivation of photocatalyst over time (Hoffmann et al., 1995; Pehkonen et al., 1993).

2.2 TiO_2 PHOTOCATALYST

Among the various semiconductors used for photocatalysis technology, TiO_2 has been approved to be the best material for environmental purification. TiO_2-based photocatalytic products covering self-cleaning, air purification, water purification and bactericidal applications have been commenced for about 20 years. Most recently, TiO_2 photocatalysis shifted into the area of hydrophillicity which involves antifogging surfaces (Fujishima et al., 2007).

TiO_2 photocatalyst has many desirable properties such as being readily available, cheap and highly stable chemically (Bryne et al., 2011). In addition to that, its highly oxidizing photogenerated holes as well as corresponding electrons with sufficient electronegativity to reduce dioxygen to superoxide/hyperoxide radicals provide oxidation of a wide range of organic compounds. The degradation of organic pollutants using TiO_2 photocatalysis mechanism with irradiation of UV light is illustrated in Fig. 2.2.

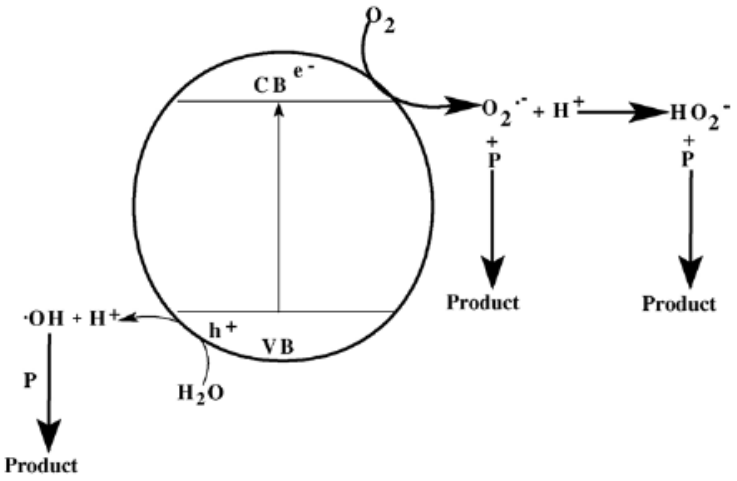

Figure 2.2. Schematic representation of UV/TiO_2 photocatalysis system (Chatterjee and Dasgupta, 2005).

There are three distinct crystal forms of TiO_2; anatase, brookite and rutile. Anatase and rutile are commonly used in photocatalysis while preparation of brookite phase is quite difficult without any anatase and rutile phase which limits its study and application (Xie et al., 2009). Figure 2.3 shows unit cell of anatase and rutile phases of TiO_2. In both phases, each Ti^{4+} ion is circulated by an octahedron of six O^{2-} ions. The octahedron in rutile shows a slight orthorhombic distortion while in anatase, it is significantly distorted. Therefore, symmetry of anatase is lower than orthorhombic. The Ti-O distances in anatase are shorter whereas Ti-Ti distances are greater than in rutile (Fahmi et al., 1993). Also, the number of contacting neighbour octahedrons in rutile and anatase structure is 10 and 8, respectively. All of these differences in lattice structures give rise to different lattice parameters and electronic band structures between two phases of TiO_2 (Linsebigler et al., 1995).

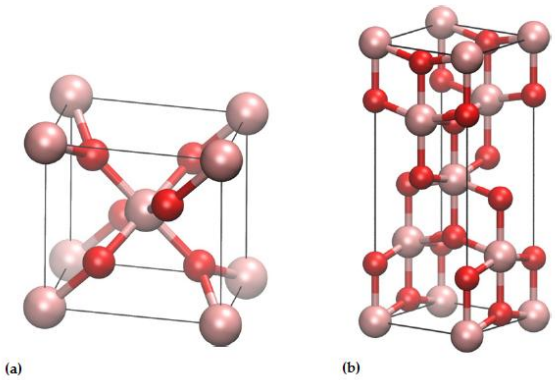

Figure 2.3. Unit cells of the TiO_2 modifications (a) Rutile, (b) Anatase. Gray atoms represent titanium and red atoms represent oxygen (Moellmann et al., 2012).

Two requirements namely, a large surface area and high crystallinity must be satisfied in order to have high photocatalytic activity. Large surface area provides effective absorption of substrates whereas high crystallinity minimizes e^- and h^+ recombination rate (Ohtani et al., 1993). Having lower band gap energy (3.02 eV) than anatase TiO_2 (3.23 eV), rutile TiO_2 is supposed to absorb organic substances more strongly than anatase near UV light region. However, difficulties in obtaining well-crystallized rutile TiO_2 powder having small crystallite size makes it a relatively poor photocatalyst due to its high e^- and h^+ recombination rate (Sun et al., 2003). Therefore, it is commonly agreed that anatase TiO_2 is more efficient photocatalyst than rutile TiO_2.

Investigations on photocatalyst TiO_2 mainly focus on modifying its band gap energy. The band gap energy of 3.2 eV indicates that semiconductor TiO_2 can be excited only by photons with wavelengths below 388 nm. As a consequence, less than 6% of solar energy is functional to achieve TiO_2 photocatalysis on the surface of Earth. Wavelength range of visible light is shown in Figure 2.4.

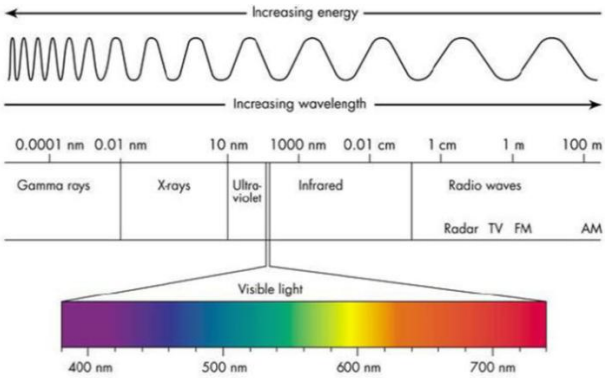

Figure 2.4. Wavelength range of visible light.

For improvement of effective utilization of light energy coming from the sun, doping metals and non-metals into TiO_2 crystal structure have been tried to prepare visible light active photocatalysts via band gap narrowing of TiO_2 photocatalyst (Kang et al., 2008). Also, photocatalysts with larger surface area is desirable for better photocatalytic performance for the reason that oxidation and reduction reactions occur on the surface of the photocatalyst. One of the most effective ways to increase surface area of TiO_2 powder is reducing its particle size. There are several preparation techniques for achievement of visible light sensitive photocatalyst TiO_2 having large surface area.

2.3 ROUTS TO IMPROVE PHOTOCATALYTIC ACTIVITY OF TiO_2

2.3.1 Particle Size Reduction

Nanoparticles have been an area of great research interest for the synthesis of new materials particularly because their processibility at low temperatures, high catalytic activity, and superior mechanical properties compared with their bulk states (Jang et al., 2001). In a photocatalytic system, reactions take place on the surface of photocatalyst particles, which must be sufficiently large for obtaining high photocatalytic activity (Lee et al., 2010). Since specific surface area of particles is directly related to their sizes, particle size plays an important role for photocatalysis. The smaller the particle size, the larger the amount of active sites on the surface, and hence the higher the rate of surface charge carriers resulting in enhanced photocatalytic activity (Zhang et al., 1998). For nanocrystalline TiO_2 based photocatalysts, photocatalytic activity is increased while TiO_2 particle size is reduced. However, it does not monotonically increase with decreasing particle size which implies that there exists an optimum particle size ranged from 7 to 45 nm for different TiO_2 and organic contaminant sources (Xu et al., 1999; Maira et al., 2000; Almquist and Biswas, 2002). For larger particle sizes than optimum size, smaller specific surface area of the particles limits the photocatalytic efficiency while for smaller crystal sizes than optimum size, optical and electronic properties of nanometer sized crystal change. Thus, existence of optimum particle size is a result of synergistic effect of specific surface area, charge-carrier dynamics and efficiency of light absorption (Koči et al., 2009).

2.3.2 Dopant Addition

As stated earlier in this chapter, one of the most active topics of research in semiconductor photocatalysis is to prepare a photocatalyst capable of using sunlight to degrade most of the synthetic and natural organic contaminants. In a reactive semiconductor particle, energy of photon is absorbed which results in generation of an e^- from the valance band to the conduction band with the concurrent generation of a h^+ in valence band (Mills and Hunte, 1997). Therefore, band structure of the semiconductor photocatalyst is crucial and must have low energy to yield an increased efficiency of photocatalytic system. Schematic illustration of the band gap structure of a semiconductor is given in Figure 2.5. In addition, photo-generated e^- and h^+ can recombine without participating in photocatalytic reactions which severely limits performance of the semiconductor photocatalysis due to low photo quantum efficiency (Cheng et al., 2012). Dopant atom addition into a particular

semiconductor photocatalyst can overcome those limitations and basically provide following benefits (Linsebigler et al., 1995).

1. Increases the wavelength response range of semiconductor photocatalyst by narrowing its band gap.
2. Inhibits recombination of e^+ and h^- by increasing charge separation.

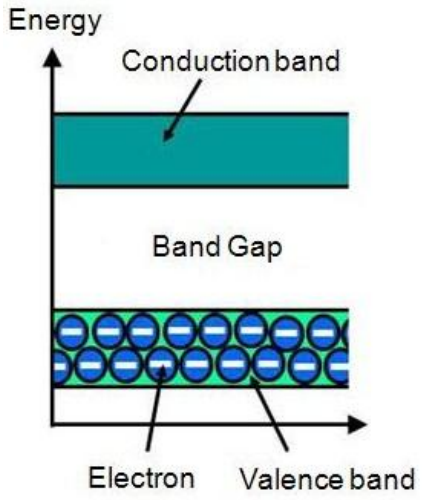

Figure 2.5. Semiconductor band gap structure.

For TiO_2 photocatalysts, the doping of nonmetal atoms can enter into lattice structure and decrease the band gap, possibly give rise to response to solar illumination, whereas doping metal atoms can suppress the recombination of photo-generated e^- and h^+ pairs during their migration from inside of the photocatalyst to the surface resulting in higher photo quantum efficiency (Ling et al., 2008; Zhang and Liu, 2008). Therefore, modifying TiO_2 photocatalyst by co-doping with metal and nonmetal cooperatively improves its photocatalytic activity further (Sakatani et al., 2003; Wei et al., 2007).

TiO_2 powders have been doped with many different metal and nonmetal atoms as reported in Chapter 1. There are only a few publications on B as a nonmetal dopant (Chen et al., 2006). The role of dopant B in TiO_2 photocatalysis still remains controversial. Improved photocatalytic performance of TiO_2 by B doping can be described with either red shift of UV absorption band to the visible region due to weaving of B atoms into TiO_2 lattice interstitially, or blue shift of UV absorption band as a result of quantization effect (Khan et al., 2008). As a transition metal, Zr is an effective dopant with their electron scavenging effect on the surface of TiO_2. Therefore, incorporation of Zr atoms in TiO_2 structure increases rate of photocatalytic oxidation (Venkatachalam et al., 2007).

This study was devoted on determining improvement in photocatalytic performance as a result of cooperative effect of B-Zr co-doping into TiO_2 powder. However, production route of B-Zr co-doped TiO_2 powder is also a critical factor for achieving a photocatalyst with

high photocatalytic activity because properties of powder and success of doping is directly related to its production technique. Several methods have been employed for doping metal and nonmetal atoms into TiO_2 lattice some of which are sol-gel process (Cernea et al., 2007; Lin et al., 2007), hydrothermal process (Tian et al., 2008; Ho et al., 2006) and mechanical ball milling (Woo et al., 2007; Park et al., 2006). Brief information about each process is given in the following section.

2.4 PREPARATION METHODS OF B-Zr CO-DOPED TiO_2 POWDER

2.4.1 Sol-gel Process

Sol-gel is the most common preparation method of nanosize TiO_2 powder with high photocatalytic activity (Hong et al., 2003). Production of TiO_2 by sol-gel process includes hydrolysis and polycondesation reactions of titanium alkoxides ($Ti(OR)_n$), to form oxopolymers transforming into an oxide network. The overall reaction can be written as (Su et al., 2004);

$$M(OR)_n + \frac{n}{2} H_2O \longrightarrow MO_{n/2} + {}_nROH$$

A solution containing dopant specie(s) is added to the mixture of titanium isopropoxide to prepare doped TiO_2 powder by sol-gel method. Also, calcination of powders prepared is essential to remove organic molecules and finalize the crystallization. Sol-gel method allows achieving superior purity and compositional homogeneity of the products at moderate temperatures with the use of simple laboratory equipment. However, the need of costly, large amount of organic substances is a drawback (Han et al., 2008; Niederberger and Pinna, 2009). In addition, high calcination temperature results in large crystallite size which negatively affects the performance of the photocatalyst (Su et al., 2004).

2.4.2 Hydrothermal Process

Hydrothermal synthesis is applied for the preparation of different nanocrystalline inorganic materials such as TiO_2 photocatalyst (Kolen'ko et al., 2004). Main mechanism of hydrothermal process involves condensation and polymerisation of precursor fragments in an aqueous solution at elevated temperature in a pressurized vessel for instance an autoclave (Nam and Han, 2003). Titanium alkoxides and alcohol are commonly used as precursor solution in a typical hydrothermal process for preparation of nanocrystalline TiO_2 powder. Acid and organic additives are also introduced to the solution to induce crystallization and inhibit agglomeration of particles (Bacsa et al., 1996). Distilled water or different mineralizers such as hydroxides, fluorides or chlorides of alkali metals can be used in hydrothermal treatment of $TiO_2 \cdot nH_2O$ amorphous gels (Kolen'ko et al., 2004). Also,

addition of selected metal or nonmetal ion precursors enable to prepare doped TiO_2 photocatalysts by hydrothermal method (Zhu et al., 2004).

Hydrothermal process provides well crystallized products, which benefits thermal stability of the materials. However, for the preparation of TiO_2, it is difficult to control ratio of various additives to get well-dispersed anatase powders. Also, removal of organic solvents and additives need further heat treatment or repeated washing (Bao et al., 2005).

2.4.3 Ball Milling

Mechanical alloying by ball milling is proved to be an efficient and simple method for the production of nanostructured powders in large quantities with modified properties (Zhang et al., 2008). In this technique, starting powder particles are captured between crashing balls and inner surface of the container results in fine and well-dispersed particles due to repeated deformation, rewelding and fragmentation of mixed powders. In ball milling process, two events; cold-welding and fragmentation occur simultaneously. During cold-welding process, colliding particles form agglomerates leads to increase in average particle size and then, breaking up of those agglomerates takes place in fragmentation process (Salah et al., 2011). Vertical view of the motion of powders, balls and container in a conventional ball mill is illustrated in Figure 2.6.

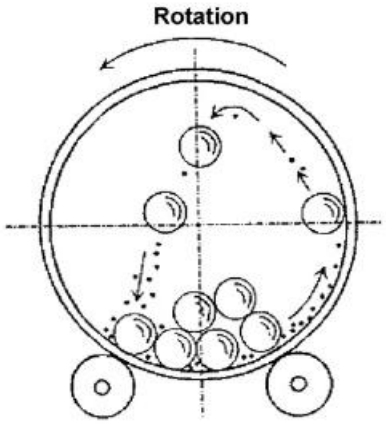

Figure 2.6. Vertical view of powders, balls and container in a conventional ball mill (Suryanarayana, 2001).

Mechanical alloying by ball milling needs optimization of different variables such as milling container, milling speed, milling time, ball-to-powder weight ratio, milling atmosphere and temperature of milling to achieve desired microstructure of product (Suryanarayana, 2001). Although there are different types of superior machineries used in ball milling process like planetary ball mill, vibration ball mill and stirred ball mill (Choi et al., 2001), conventional ball mill is found to be easier in controlling milling parameters.

Recently, ball milling process is applied for synthesizing metal and nonmetal doped nanosized TiO_2 powders which showed excellent photocatalytic activities due to beneficial effects of dopant addition and reduction of particle size of powder at the same time (Fan et al., 2009; Uhm et al., 2006; Shifu et al., 2006).

CHAPTER 3

EXPERIMENTAL PROCEDURE

3.1 POWDER PREPARATION

A commercially available metatitanate ($TiO_2.H_2O$) powders was taken as TiO_2 source due to the fact that particle size reduction and co-doping in this powder would be easier than that in fully crystallized TiO_2 powders. Starting $TiO_2.H_2O$ powder was purchased from Nano Co. It has particles size less than 1 μm in size. Boric acid (H_3BO_3) and zirconium acetylacetonate ($Zr(C_5H_7O_2)_3$) purchased from Sigma-Aldrich were used as dopant source for B and Zr doping, respectively. Agglomeration of particles during ball milling process was prevented by the help of Darvan C-N (Vanderbilt Co.) dispersant. All chemicals used in this study were analytically grade and used in as received from without any purification or treatment.

A conventional type of ball mill equipped with zirconia (ZrO_2) jar was employed in powder preparation steps to obtain well-dispersed, refined and doped TiO_2 powders. The inner volume of the jar was 250 mL. In order to reduce contamination resulting from balls and inner surface of the jar due to abrasion, ZrO_2 balls with a diameter of 1 mm were utilized. Wet milling was carried out with deionized water as the wetting media. All other milling parameters used throughout in this study are listed in Table 3.1.

Table 3.1. Parameters used in ball milling process throughout this study.

Milling speed (rpm)	450
Milling time (h)	24
Ball-to-powder ratio	1:40
Amount of dispersant (mL)	5

Starting powder was ball milled with B and/or Zr dopants to obtain B-doped, Zr-doped, and B-Zr co-doped TiO_2 powders. Starting powder was also ball milled without any dopant addition to see the effect(s) of particle size reduction independently on photocatalytic properties. The experimental procedure for the preparation of B-doped, Zr-doped, and B-Zr co-doped TiO_2 powders will be explained in the subsections below.

3.1.1 Preparation of B doped TiO_2 powder

B doped TiO_2 powders were prepared by ball milling starting metatitanate powder with various amount of H_3BO_3. Necessary amount of H_3BO_3 was added to TiO_2 powders to yield B doping of 0.5, 1.0, and 1.5 weight percent (wt%). B-doped TiO_2 powders were labelled "B_x-TiO_2", where x represents the B concentrations in terms of wt%. In the preparation of a typical B-doped TiO_2 powder (e.i. $B_{0.5}$-TiO_2), first a solution was prepared by mixing 0.58 g H_3BO_3 with 50 mL deoinized water. Then, this solution was added drop wise to a mixture formed from 25 g of $TiO(OH)_2$ and 150 mL of deionized water and stirred magnetically. Since ball-to-powder ratio was 1:40, 1000 g of ZrO_2 balls and the suspension obtained were put in a ZrO_2 jar. After addition of 5 mL dispersant into the jar, ball milling was carried out continuously at 450 rpm for 24 h. After that, the ball milled suspension was dried in an oven at 105° C for 15 h to obtain powder. The powders obtained were mechanically ground by the use of agate mortar with pestle. Finally, the resulting dry powders were calcined at 200 °C for 30 min to remove organics and allow the diffusion of dopant material. The heating rate was 2 °C/min. After calcination, powders cooled at a rate of 2 °C/min were $B_{0.5}$-TiO_2 powders. The flowchart showing the experimental procedure for the preparation of $B_{0.5}$-TiO_2 powder is illustrated in Figure 3.1. $B_{1.0}$-TiO_2 and $B_{1.5}$-TiO_2 powders were prepared in the same manner but by increasing the H_3BO_3 amount to 1.16 g and 1.74 g, respectively.

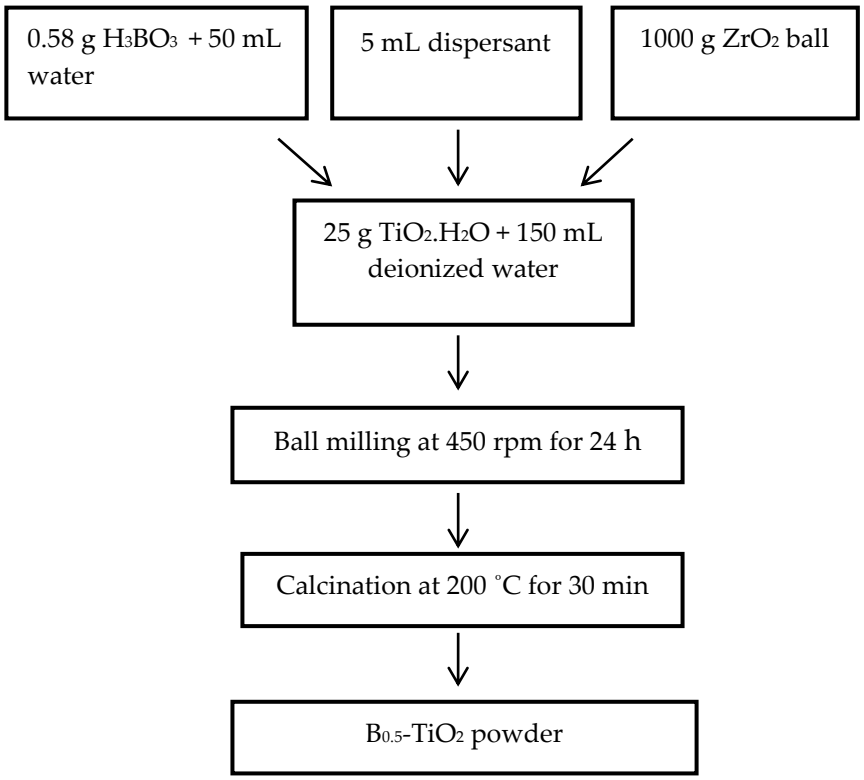

Figure 3.1. Flowchart of the experimental procedure for the preparation $B_{0.5}$-TiO_2 powder.

3.1.2 Preparation of Zr doped TiO_2 powder

Zr-doped TiO_2 powders were prepared in the same manner but by replacing H_3BO_3 solution with $Zr(C_5H_7O_2)_3$ solution. Zr-doped powders were labeled "Zr_y-TiO_2", where y represents the Zr concentration and varied from 0.5 wt% to 1.5 wt% with 0.5% increments. Since $Zr(C_5H_7O_2)_3$ is not soluble in water, ethanol (EtOH) was used instead of water. In the preparation of a typical Zr-doped TiO_2 powder (e.i. $Zr_{0.5}$-TiO_2), first a solution was prepared by mixing 0.43 g of $Zr(C_5H_7O_2)_3$ with 50 mL EtOH. Then, this solution was added drop wise to a mixture formed from 25 g of $TiO(OH)_2$ and 150 mL of deionized water and stirred magnetically. ZrO_2 balls and the suspension obtained were put in a ZrO_2 jar. After addition of 5 mL dispersant into the jar, ball milling was carried out continuously. After that, the ball milled suspension was dried in an oven at 105° C for 15 h to obtain powder. The powders obtained were mechanically ground by the use of agate mortar with pestle. Finally, the dry powders were calcined at 200 °C for 30 min. The heating rate was 2 °C/min. After calcination, powders cooled at a rate of 2°C/min were $Zr_{0.5}$-TiO_2 powders. The flowchart showing the experimental procedure for the preparation of $Zr_{0.5}$-TiO_2 powder is illustrated in Figure 3.2. $Zr_{1.0}$-TiO_2 and $Zr_{1.5}$-TiO_2 powders were prepared in the same manner but by increasing the amount of $Zr(C_5H_7O_2)_3$ to 0.86 g and 1.29 g, respectively.

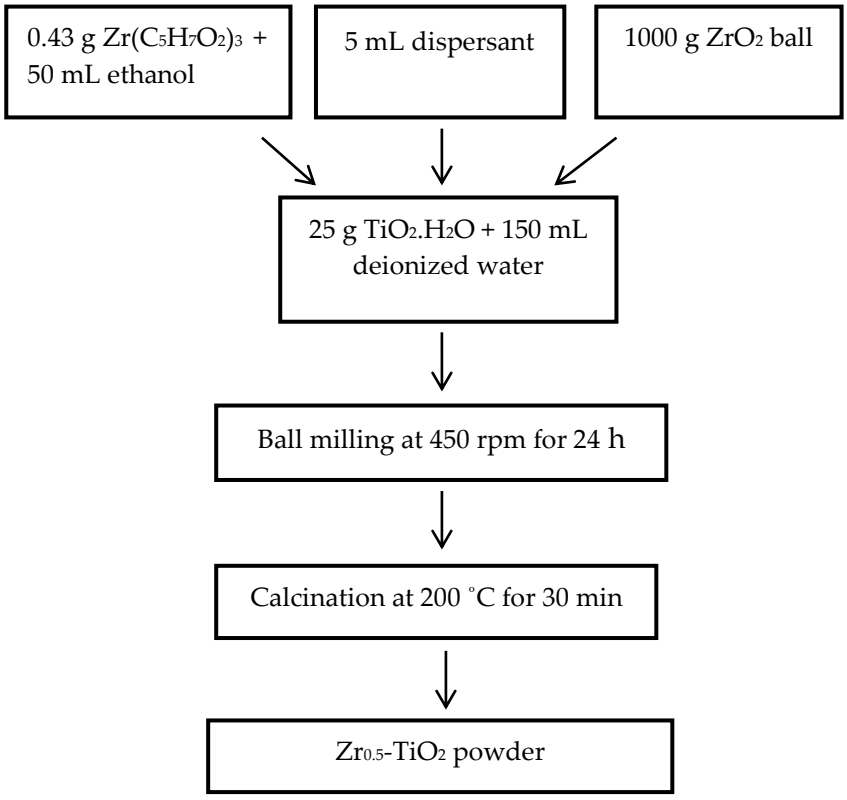

Figure 3.2. Flowchart of the experimental procedure for the preparation of $Zr_{0.5}$-TiO_2 powder.

3.1.3 Preparation of B-Zr co-doped TiO_2 powder

B-Zr co-doped TiO_2 powders were prepared in the same manner but by mixing the solutions of H_3BO_3 in deionized water, and $Zr(C_5H_7O_2)_3$ in EtOH. These powders were prepared by keeping the B concentration constant at 0.5 wt% and varying the Zr concentrations from 0.3 wt% to 0.7 wt% with 0.2% increments, and labeled "$B_{0.5}$-Zr_z-TiO_2", where z represents the Zr concentration. In the preparation of a typical B-Zr co-doped TiO_2 powder (e.i. $B_{0.5}$-$Zr_{0.3}$-TiO_2), first solutions prepared by mixing 0.58 g H_3BO_3 with 50 mL deoinized water, and 0.43 g of $Zr(C_5H_7O_2)_3$ with 50 mL EtOH were added drop wise to a mixture formed from 25 g of $TiO(OH)_2$ and 150 mL of deionized water and stirred magnetically. ZrO_2 balls and the suspension obtained were put in a ZrO_2 jar. After addition of 5 mL dispersant into the jar, ball milling was carried out continuously. After that, the ball milled suspension was dried in an oven at 105° C for 15 h to obtain powder. The powders obtained were mechanically ground by the use of agate mortar with pestle. Finally, the dry powders were calcined at 200 °C for 30 min. The heating rate was 2 °C/min. After calcination, powders cooled at a rate of 2°C/min were $B_{0.5}$-$Zr_{0.3}$-TiO_2 powders. The flowchart showing the experimental procedure for the preparation of $Zr_{0.5}$-TiO_2 powder is illustrated in Figure 3.3. $B_{0.5}$-$Zr_{1.0}$-TiO_2 and $B_{0.5}$-$Zr_{1.5}$-TiO_2 powders were prepared in the same manner but by increasing the amount of $Zr(C_5H_7O_2)_3$ to 0.86 g and 1.29 g, respectively.

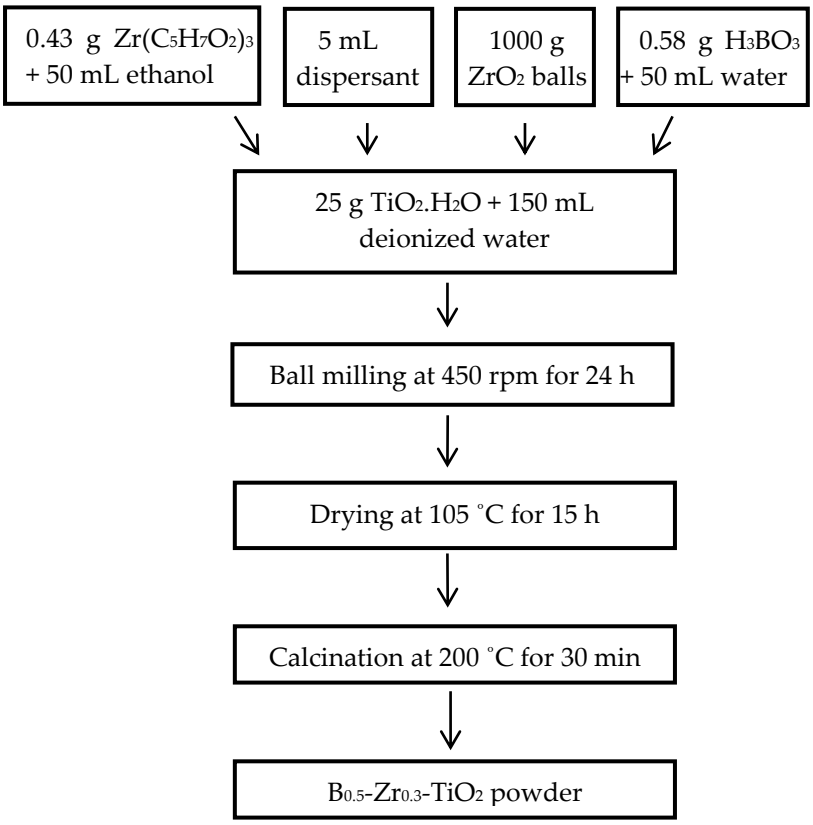

Figure 3.3. Flowchart of the experimental procedure for the preparation of $B_{0.5}$-$Zr_{0.3}$-TiO_2 powder.

3.2 CHARACTERIZATION

3.2.1 X-Ray Diffraction (XRD) Analysis

XRD analysis was performed to identify the phases present in as received, milled, B-doped, Zr-doped, and B-Zr co-doped TiO_2 powders. A Rigaku-Geigerflex DMAK/B X-ray diffractometer equipped with Cu target Kα radiation as X-ray source was used to get XRD patterns of the powders. Each powder was scanned in a 2θ range of 20° - 80° at a rate of 2°/min by 0.02° increments continuously with an accelerating voltage of 40 kV and applied current of 40 mA.

XRD patterns of the powders were refined using EXPGUI, a graphical interface of GSAS (Toby, 2001) by the Rietveld refinement method to obtain accurate lattice parameters of the powders as well as positions of the atoms in the crystal structure of TiO_2. Thus, effect of the B and/or Zr doping in TiO_2 lattice and doping mechanism could be explained with the help of this refinement technique. Also, Rietveld refinement was performed to get data for the average particle size of TiO_2 powders.

3.2.2 X-ray Photoelectron Spectroscopy (XPS) Analysis

In order to investigate the surface composition and chemical state of the TiO_2 powders prepared, XPS analysis was performed on the SPECS spectrometer (EA 300) with Al Kα radiation. Detailed XPS scans were obtained for B 1s, Zr 3d and Ti 2p to recognize whether dopant atoms weaved into crystal lattice of TiO_2 or formed various compounds with Ti, O, and dopant elements. Doped atoms at the surface of TiO_2 were analysed by means of binding energies obtained from XPS technique.

3.2.3 Scanning Electron Microscope (SEM) and Energy Dispersive Spectroscopy (EDS) Analyses

A Nova NANOSEM 430 scanning electron microscope was employed to examine surface morphology and estimate the particle size of the TiO_2 powders prepared. Also, in order to observe presence of the B and Zr atoms, elemental analysis was performed by EDS. Powders containing Zr were coated with carbon (C) instead of gold (Au) since peaks of Au and Zr overlap in EDS spectrum.

3.3 PHOTOCATALYTIC ACTIVITY MEASUREMENT

Photocatalytic activity measurement of the powders prepared was carried out inside a fully dark wooden box without letting any leakage of sun light. The box is equipped with a Black-Ray-grade UV semiconductor lamp with a power of 100W, a self-designed vessel, and a magnetic stirrer. The vessel located at 10 cm below the UV lamp was steeped in a

thermostatic circulation bath to prevent sudden temperature changes due to warm up of the lamp and exothermic photocatalytic reactions. Scinco S-3100 UV-Vis single beam spectrophotometer was used for the photocatalytic activity measurements.

In order to evaluate photocatalytic performance, methylene blue (MB) solution was taken as pollutant model. A 10 mg/L MB aqueous solution was prepared by dissolving 0.01 g MB powder in 1 L of deionized water. A 10 mg of TiO_2 powder was added into self-designed vessel containing 200 mL of MB solution and the resulting suspension was continuously stirred magnetically during the experiment. For the first 30 min, stirring was done in the dark for the purpose of reaching adsorption/desorption equilibrium of MB solution. At the end of first 30 min, 4 mL of suspension was syringed and then transferred into a quartz cuvette by using Millex Millipore syringe filter with a mesh size of 0.22 μm to obtain a clear, powder free sol for the UV-vis spectrophotometer measurement. Then, UV light source was turned on and after 90 min another 4 mL sample was taken in the same manner as described above. Absorbance values of the two samples were determined at characteristic wavelength (λ = 664 nm) of MB from spectrophotometer results. The photocatalytic activity is evaluated by using the formula (Ling et al., 2008);

$$\text{Degradation ratio (\%)} = \frac{(A0-A)}{A0} \times 100$$

A0 = Absorbance value before irradiation
A = Absorbance value at radiation time *t*

The flowchart of the photocatalytic activity measurement procedure of the TiO_2 powders prepared is shown in Figure 3.4.

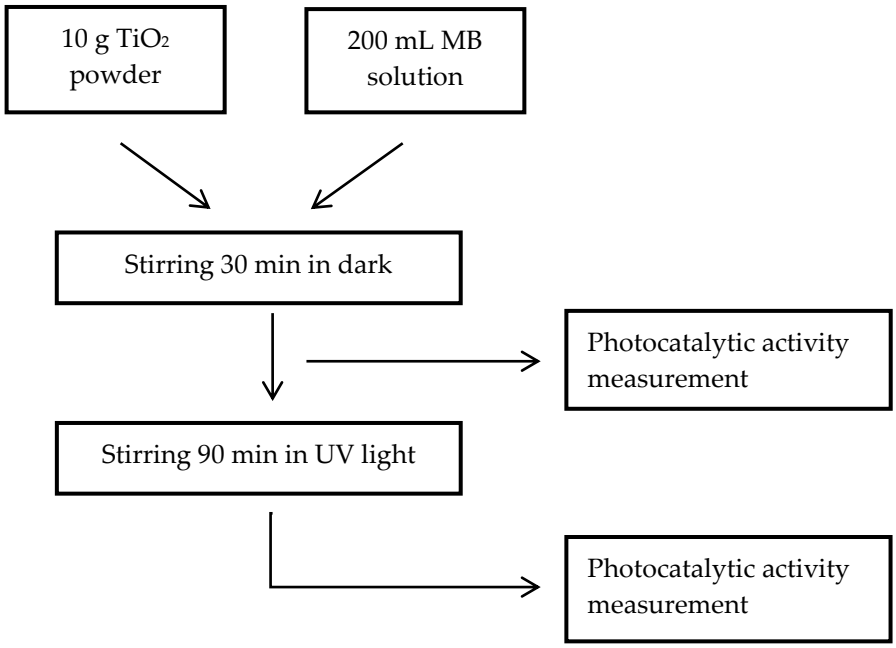

Figure 3.4. The flowchart of the photocatalytic activity measurement process.

CHAPTER 4

RESULTS AND DISCUSSION

4.1 GENERAL REMARKS

In this chapter, data gathered from the experimental studies were presented and results were discussed.

In addition to the starting $TiO_2.H_2O$ powder referred to as as-received TiO_2, 11 different TiO_2 powders were prepared and subjected to characterization and photocatalytic activity measurement tests. All of the powders used throughout this study and their labels are listed in Table 4.1. The starting $TiO_2.H_2O$ powder milled without any dopant addition was referred to as milled $TiO_2.H_2O$. The starting $TiO_2.H_2O$ powder milled without any dopant addition and calcined at 200 °C was referred to as milled TiO_2. 9 of the TiO_2 powders prepared were the starting $TiO_2.H_2O$ powder doped or co-doped with B and/or Zr.

Table 4.1. The powders used throughout this study and their names.

Powder	**Label**
Starting $TiO_2.H_2O$	As-received TiO_2
Starting $TiO_2.H_2O$ milled without any dopant addition	Milled $TiO_2.H_2O$
Starting $TiO_2.H_2O$ milled without any dopant addition and calcined at 200 °C	Milled TiO_2
0.5 wt% B-doped $TiO(OH)_2$	$B_{0.5*}$-TiO_2
1.0 wt% B-doped $TiO(OH)_2$	$B_{1.0}$-TiO_2
1.5 wt% B-doped $TiO(OH)_2$	$B_{1.5}$-TiO_2
0.5 wt% Zr-doped $TiO(OH)_2$	$Zr_{0.5}$-TiO_2
1.0 wt% Zr-doped $TiO(OH)_2$	$Zr_{1.0}$-TiO_2
1.5 wt% Zr-doped $TiO(OH)_2$	$Zr_{1.5}$-TiO_2
0.5 wt% B-doped and 0.3 wt% Zr-doped $TiO(OH)_2$	$B_{0.5}$-$Zr_{0.3}$-TiO_2
0.5 wt% B-doped and 0.5 wt% Zr-doped $TiO(OH)_2$	$B_{0.5}$-$Zr_{0.5}$-TiO_2
0.5 wt% B-doped and 0.7 wt% Zr-doped $TiO(OH)_2$	$B_{0.5}$-$Zr_{0.7}$-TiO_2

* Intended dopant amount.

B-doped TiO_2 powders prepared by 0.5, 1.0, 1.5 wt% B addition were labelled as $B_{0.5}$-TiO_2, $B_{1.0}$-TiO_2, and $B_{1.5}$-TiO_2, respectively. Zr-doped TiO_2 powders prepared by 0.5, 1.0 and 1.5 wt% Zr addition were labelled as $Zr_{0.5}$-TiO_2, $Zr_{1.0}$-TiO_2, and $Zr_{1.5}$-TiO_2, respectively. B-Zr co-doped TiO_2 powders prepared by constant 0.5 wt% B addition and 0.3, 0.5 and 0.7 wt% Zr additions were labelled as $B_{0.5}$-$Zr_{0.3}$-TiO_2, $B_{0.5}$-$Zr_{0.5}$-TiO_2, and $B_{0.5}$-$Zr_{0.7}$-TiO_2, respectively. Hereafter, the powders will be referred in the text according to their labelled names unless otherwise is mentioned.

4.2 CHARACTERIZATION

4.2.1 X-Ray Diffraction (XRD)

The XRD patterns of as-received TiO_2, milled $TiO_2.H_2O$, milled TiO_2 powders suggest that the powders are composed of only anatase TiO_2 identified by the characteristic (101) diffraction peak at 2θ of ~25.3° (JCPDS #21-1272) as shown in Figure 4.1. The XRD analysis revealed that as-received and milled $TiO_2.H_2O$ powders did not exhibit any amorphous structure due to crystal water in $TiO_2.H_2O$. An increase in the peak intensities of milled TiO_2 powders in the XRD pattern signifies that fully crystalline anatase TiO_2 powders are obtained from as-received $TiO_2.H_2O$ powders after milling and calcination at 200 ˚C. Similar results have been reported by Li et al., 2011. A comparison of the XRD peaks of as-received and milled $TiO_2.H_2O$ powders implies that the peaks of milled powder are broadened due to the major effect of ball milling process. Furthermore, it is clear that the peak diffracted from (101) crystal plane shifted to lower diffraction angle for the milled $TiO_2.H_2O$ powder as a result of distortion created in the lattice of TiO_2 by high energy of ball milling as best seen in the inset in Figure 4.1.

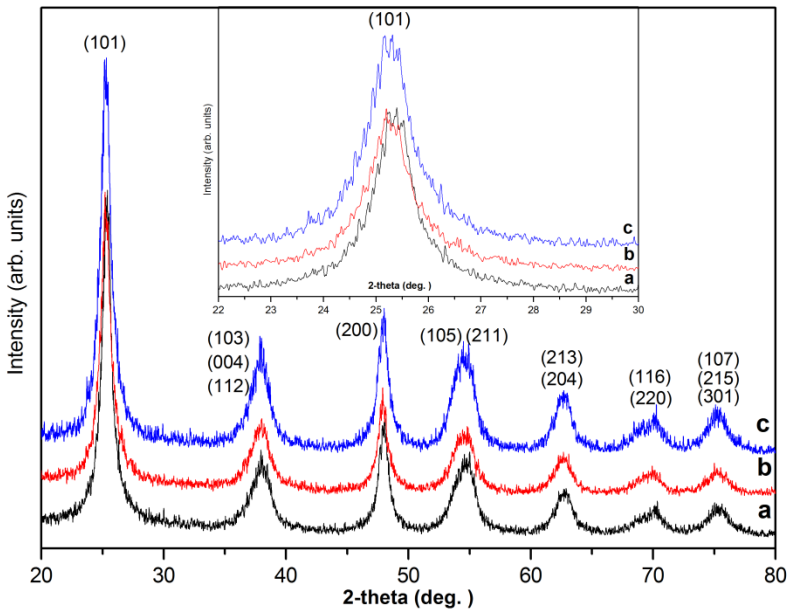

Figure 4.1. XRD patterns for powders of (a) as-received TiO_2, (b) milled $TiO_2.H_2O$, and (c) milled TiO_2.

For the purpose of investigating the effect of dopant(s) atoms on the phases present in the B-doped, Zr-doped, and B-Zr co-doped TiO_2 powders, milled TiO_2 powder was taken as reference powder. The XRD pattern of milled TiO_2 powder was compared with the XRD patterns of the doped and co-doped TiO_2 powders. The XRD patterns of milled TiO_2 and B-doped TiO_2 powders are shown in Figure 4.2.

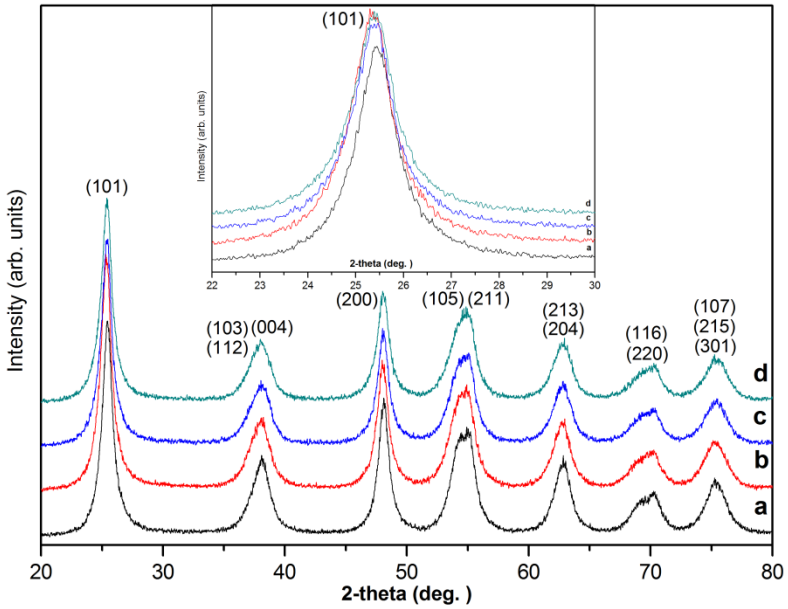

Figure 4.2. XRD patterns for powders of (a) milled TiO_2, (b) $B_{0.5}$-TiO_2, (c) $B_{1.0}$-TiO_2 and (d) $B_{1.5}$-TiO_2.

The XRD analysis revealed that B-doped TiO_2 powders composed of only anatase TiO_2 and did not exhibit any additional phase related to B species. The XRD patterns indicate the characteristic (101) diffraction peak of anatase TiO_2 at 2θ of ~25.3°. A comparison of the XRD patterns between the JCPDS card of anatase TiO_2 and B-doped TiO_2 powders implies that TiO_2 kept the anatase structure after doping with B ions. Detection of no new phase in the XRD patters of B-doped TiO_2 powders may be due to two reasons. First, the concentration of the B dopant was so low that XRD was not sufficient to detect the new phase(s). Second, B ions incorporated into the lattice of TiO_2 and occupied some of the Ti or O lattice sites. It is clear that dopant B atoms shifted the peaks diffracted from (101) crystal plane to lower diffraction angles as best seen in the inset in Figure 4.2. This may be as a result of the further distortion created by dopant B ions in the lattice structure of TiO_2, which will be discussed in detail later after the results of Rietveld refinement analysis.

The XRD patterns of milled TiO_2 and Zr-doped TiO_2 powders are shown in Figure 4.3.

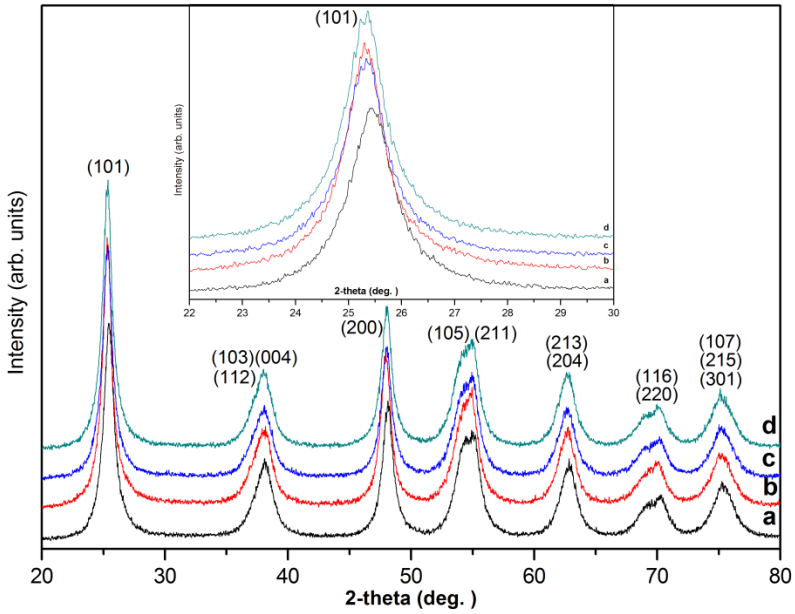

Figure 4.3. XRD patterns for powders of (a) milled TiO_2, (b) $Zr_{0.5}$-TiO_2, (c) $Zr_{1.0}$-TiO_2, and (d) $Zr_{1.5}$-TiO_2.

The XRD analysis revealed that Zr-doped TiO_2 powders composed of anatase TiO_2 and did not exhibit any additional phase related to Zr species. The patterns indicate the characteristic (101) diffraction peak of anatase TiO_2 at 2θ of ~25.3°. A comparison of the XRD patterns between the JCPDS card of anatase TiO_2 and Zr-doped TiO_2 powders implies that TiO_2 kept the anatase structure after doping with Zr ions. Detection of no new phase in the XRD patters of Zr-doped TiO_2 powders may be due to two reasons. First, the concentration of the Zr dopant was so low that XRD was not sufficient to detect the new phase(s). Second, Zr ions incorporated into the lattice of TiO_2 and occupied some of the Ti or O lattice sites. It is clear that dopant Zr atoms shifted the peaks diffracted from (101) crystal plane to lower diffraction angles as best seen in the inset in Figure 4.3. This may be as a result of the further distortion created by dopant Zr ions in the lattice structure of TiO_2, which will be discussed in detail later after the results of Rietveld refinement analysis.

The XRD patterns of milled TiO_2 and B-Zr co-doped TiO_2 powders are shown in Figure 4.4.

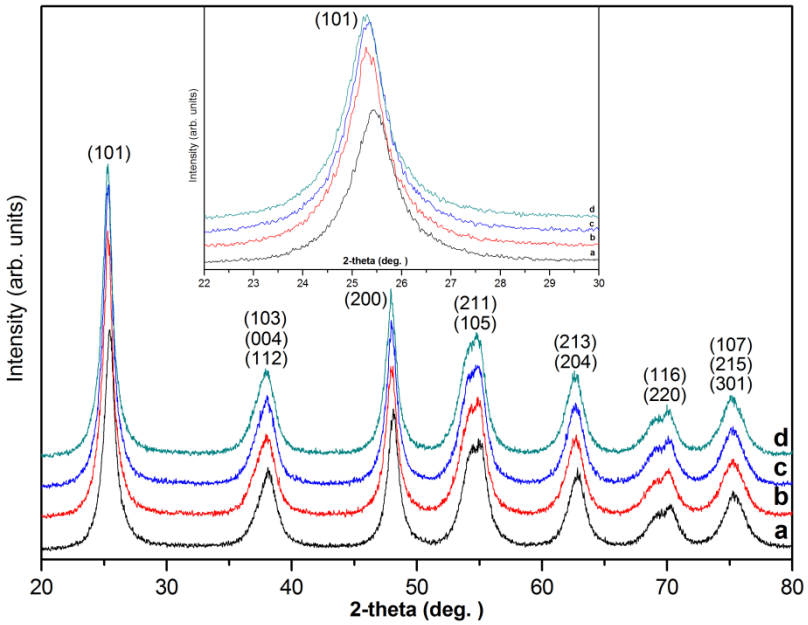

Figure 4.4. XRD patterns for powders of (a) milled TiO_2, (b) $B_{0.5}$-$Zr_{0.3}$-TiO_2, (c) $B_{0.5}$-$Zr_{0.5}$-TiO_2 and (d) $B_{0.5}$-$Zr_{0.7}$-TiO_2

The XRD analysis revealed that B-Zr co-doped TiO_2 powders composed of anatase TiO_2 and did not exhibit any additional phase related to B and/or Zr species. The patterns indicate the characteristic (101) diffraction peak of anatase TiO_2 at 2θ of ~25.3°. A comparison of the XRD patterns between the JCPDS card of anatase TiO_2 and B-Zr co-doped TiO_2 powders implies that TiO_2 kept the anatase structure after doping with B and Zr ions. Detection of no new phase in the XRD patters of Zr-doped TiO_2 powders may be due to the reasons that first, the concentrations of the dopants were so low that XRD was not sufficient to detect the new phase(s) or second, B ions and Zr ions incorporated into the lattice of TiO_2 and occupied some of the Ti or O lattice sites. It is clear that dopant atoms shifted the peaks diffracted from (101) crystal plane to lower diffraction angles as best seen in the inset in Figure 4.4. This may be as a result of the further distortion created by dopant B and Zr ions in the lattice structure of TiO_2, which will be discussed in detail later after the results of Rietveld refinement analysis.

Full-profile refinement was performed on diffraction patterns for doped and co-doped TiO_2 powders by the Rietveld method which uses non-linear least squares to minimize the difference between experimental and calculated peak intensities. In order to indicate effect(s) of doping in the lattice of TiO_2 clearly, XRD pattern of milled TiO_2 powder was also refined. The refinement results obtained were compared with those of the doped and co-doped TiO_2 powders. The counting statistics of Rietveld method is valid only when collecting X-Ray data by using fixed divergence slits. However, in this study, all of the X-Ray data were obtained by using variable divergence slits which necessitates correction of the data before starting Rietveld analysis. For that reason, intensity values of the peaks were divided by sinus of its diffraction angle to approximately correct the error due to wrong slit selection according the formula given by Winburn, 2003;

$$I(obs) = I(abs) \ \ sin\,\theta$$

I(abs) = Absolute value of intensity
I(obs) = Observed intensity (corrected)

XRD analysis clarified that all of the powders were in anatase form of TiO_2. Since anatase TiO_2 has tetragonal symmetry, as-received TiO_2 powder belongs to space group of $I4_1/amd$ (Hahn, 2005) with the lattice parameters of a = b = 3.7867 Å and c = 9.5149 Å (Weirich et al., 2000). The atomic coordinates of Ti and O atoms in TiO_2 lattice are taken as (0, 0.7500, 0.1250) and (0, 0.7500, 0.3333), respectively (Manik et al., 2003). In order to have better refinement, dual Cu Kα radiation was selected as an instrument parameter having primary and secondary wavelength values of 1.54060 Å and 1.54439 Å, respectively. Also, polarization correction was selected as diffracted beam with a polarization factor of 0.7. Well-refined XRD pattern according to refinement parameters mentioned above for milled TiO_2 is shown in Figure 4.5 where the '●' signs represent experimental points, solid line represents Rietveld refined data, dotted lines are the difference between experimental and refined data.

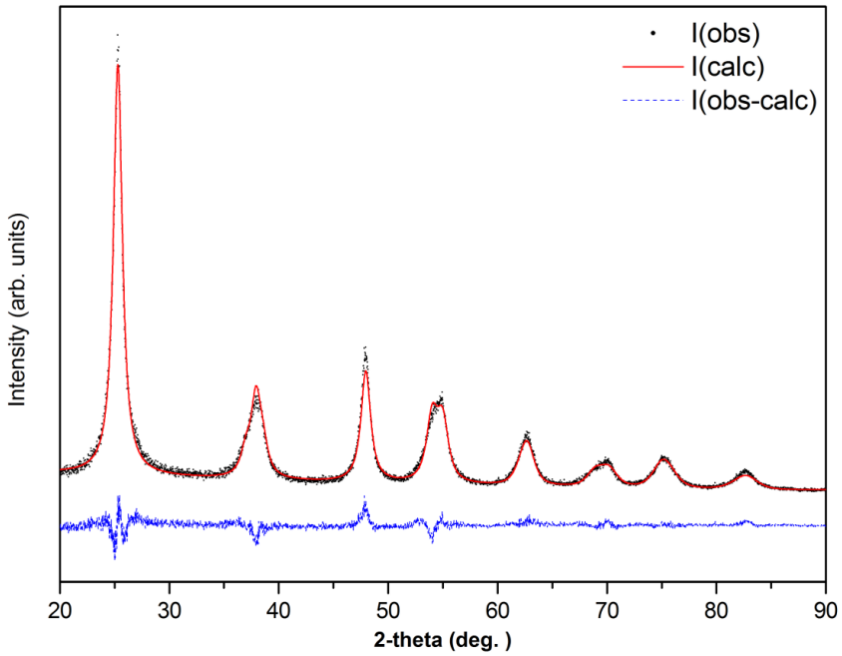

Figure 4.5. XRD pattern along with Rietveld refined data for milled TiO_2.

Before the refinement of B-doped TiO_2 powders, it was assumed that dopant B atoms will be directly substituted by O atoms in TiO_2 lattice and 4 % of O lattice sites will be occupied (Geng et al., 2006). Therefore, atomic position of B atoms which is identical to that of O atoms was taken as 0, 0.7500, 0.3333 with an occupancy value of 0.04. XRD patterns along with Rietveld refined data obtained according to these parameters for B-doped TiO_2 powders are shown in Figure 4.6.

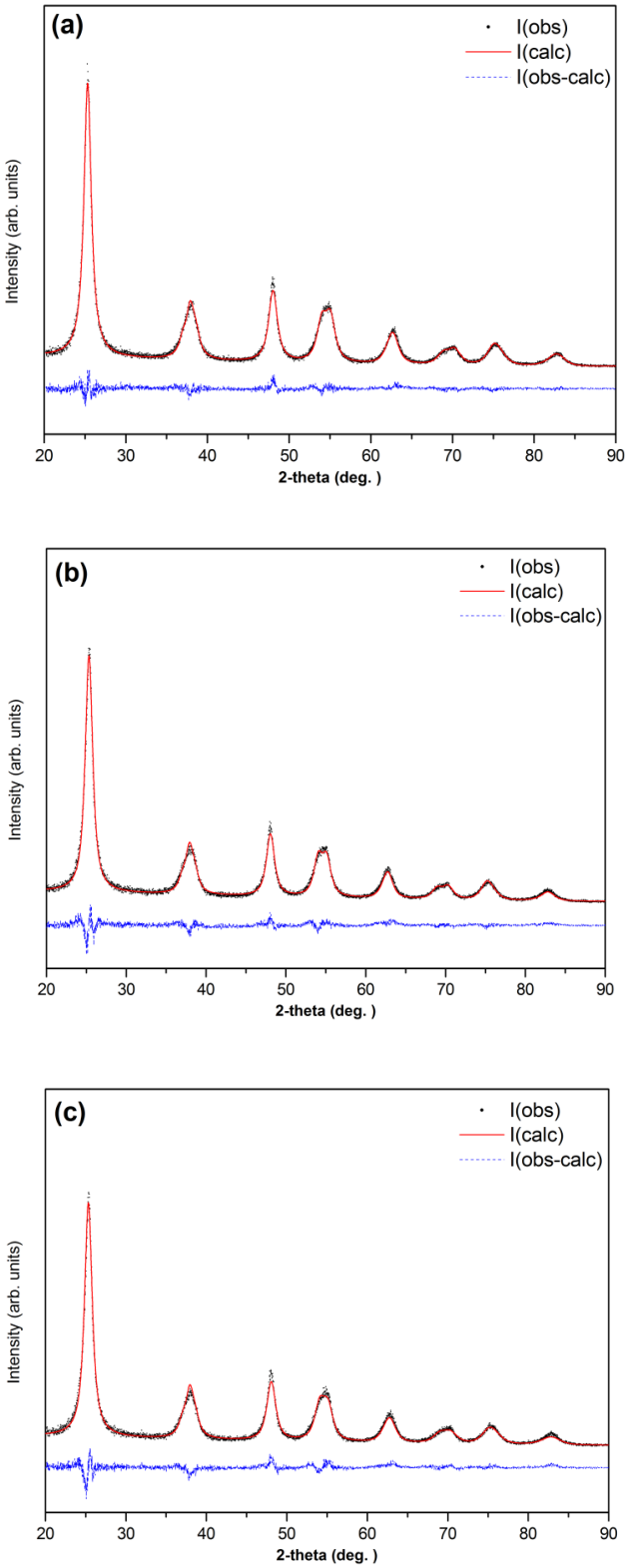

Figure 4.6. XRD patterns along with Rietveld refined data for the powders of (a) $B_{0.5}$-TiO_2, (b) $B_{1.0}$-TiO_2, and (c) $B_{1.5}$-TiO_2.

The values of refinement parameters obtained by Rietveld analysis for milled TiO_2 and B-doped TiO_2 powders are tabulated in Table 4.2.

Table 4.2. Refinement parameters of milled TiO_2 and B-doped TiO_2 powders.

Refinement Parameters	**Milled TiO_2**	**$B_{0.5}$-TiO_2**	**$B_{1.0}$-TiO_2**	**$B_{1.5}$-TiO_2**
Space group	$I4_1/amd$	$I4_1/amd$	$I4_1/amd$	$I4_1/amd$
Ti (occup.)	1.0000	1.0000	1.0000	1.0000
O (occup.)	1.0000	1.0000	1.0000	1.0000
B (occup.)	-	0.2204	0.0750	0.0647
a = b (Å)*	3.7907	3.7899	3.7883	3.7895
c (Å)*	9.4838	9.5018	9.4995	9.4899
Volume ($Å^3$)	136.27	136.48	136.33	136.28
$\chi 2$ **	8.226	6.607	7.922	7.734
Rp (%) **	7.29	6.54	7.74	7.80
Rwp (%) **	9.35	8.50	9.79	9.78

* *a,b and c are lattice parameters.*

** *$\chi 2$, Rp and Rwp are the measure of goodness of the Rietveld fitting.*

Refinement continues till convergence was achieved with the value of quality factor approaching 1, which leads to define the value of GoF (Dutta et al., 2002; Larson and Von Dreele, 2004).

$$\text{GoF} = \text{Rwp} \quad \text{expected Rwp} = \sqrt{\chi 2}$$

From the plots of I(obs-calc) in Figures 4.5 and 4.6, it is clearly seen that XRD patterns of the B-doped TiO_2 powders have fitted well to the refined data. Excluding the peak positions, I(obs-calc) plots are almost linear. The GoF values of milled TiO_2 and B-doped TiO_2 powders (2.57 and 2.86, respectively) are close to 1, which also signifies the good quality of fitting.

Substitution of B^{3+} with lattice O^{2-} leads to a decrease in cell volume of TiO_2 since the radius of B^{3+} (0.023 nm) is smaller than O^{2-} (0.132 nm). Therefore, a shift in the diffraction peaks to larger diffraction angles is expected (Yuan et al., 2011). However, it has been consistently observed in this study that diffraction peaks of B-doped TiO_2 powders shifted to lower diffraction angles when compared with those of milled TiO_2 powders as seen in the inset in Figure 4.2. Furthermore, refined values of cell volume in Table 4.2 confirm that incorporation of B ions into lattice of TiO_2 give rise to additional distortion and increase in

cell volume of TiO_2. The increase in cell volume of TiO_2 implies that B^{3+} ions integrated the lattice of TiO_2 not substitutionally but interstitially. In interstitial position, B atom and three close O atoms form a planar structure in TiO_2 lattice, hence interstitial B atom adopts sp^2 hybridization (Geng et al., 2006) as illustrated in Figure 4.7.

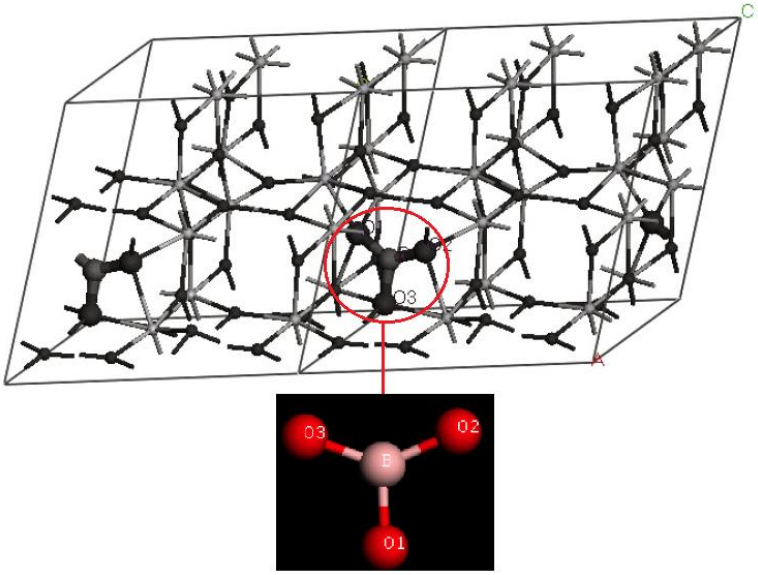

Figure 4.7. Cell structure of interstitially B-doped anatase TiO_2 (Geng et al., 2006).

Interstitial position of B atoms in TiO_2 lattice is further supported by fractional atomic positions obtained by Rietveld analysis as shown in Table 4.3.

Table 4.3. Fractional atomic positions of milled TiO_2 and B-doped TiO_2 powders.

	Ti (x, y, z) 4*a*	**O (x, y, z) 8*e***	**B (x, y, z) 8*e***
As-received TiO_2	0, 0.7500, 0.1250	0, 0.7500, 0.3333	-
Milled TiO_2	0, 0.7500, 0.1250	0, 0.7500, 0.3333	-
$B_{0.5}$-TiO_2	0, 0.7500, 0.1250	0, 0.7500, 0.3333	0, 0.7500, 0.2679
$B_{1.0}$-TiO_2	0, 0.7500, 0.1250	0, 0.7500, 0.3333	0, 0.7500, 0.2645
$B_{1.5}$-TiO_2	0, 0.7500, 0.1250	0, 0.7500, 0.3333	0, 0.7500, 0.2731

Rietveld analysis clarified that B atoms present in TiO_2 lattice have different atomic positions than Ti and O atoms. This result is an evidence of particular interstitial atomic

position of B in TiO_2 lattice. New atomic position has a definition in $I4_1/amd$ space group symmetry as multiplicity of '*8*' and Wyckoff notation of '*e*' (Hahn, 2005). It has been also noted that atomic position of B atoms changes as the B doping to TiO_2 lattice is increased.

Data obtained from Rietveld refinement analysis were imported to a computer software program named DRAWXtl to illustrate 3-D crystal structure of B-doped TiO_2 powders. A typical 3-D crystal structure of $B_{0.5}$-TiO_2 powder is shown in Figure 4.8.

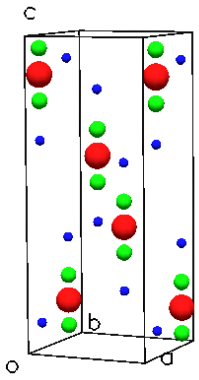

Figure 4.8. 3-D representation of the crystal structure of $B_{0.5}$-TiO_2 powder. Red atoms are Ti, blue atoms are O, and green atoms are B.

A comparison of cell volume (136.27 $Å^3$) of milled TiO_2 powder with that of $B_{0.5}$-TiO_2, $B_{1.0}$-TiO_2, and $B_{1.5}$-TiO_2 powders (136.48, 136.33, and 136.28 $Å^3$, respectively) suggests that B doping into TiO_2 lattice results in further distortion in the cell. Among B-doped TiO_2 powders, the highest distortion in TiO_2 lattice and the biggest change in cell volume were obtained by 0.5 wt% B doping. The decrease in cell volume of TiO_2 with increasing B doping could be due to the incorporation of B^{3+} ions to the TiO_2 lattice not only interstitially but also substitutionally. This judgement is also supported by occupancy values of B atoms as shown in Table 4.2. B occupancy values in $B_{0.5}$-TiO_2, $B_{1.0}$-TiO_2, and $B_{1.5}$-TiO_2 powders were 0.2204, 0.0750, and 0.0647, respectively. Dopant B atoms have occupied more interstitial lattice site in $B_{0.5}$-TiO_2 powder than in $B_{1.0}$-TiO_2 and $B_{1.5}$-TiO_2 powders meaning that more B atoms were introduced to the lattice of TiO_2 during ball milling in $B_{0.5}$-TiO_2 powder as compared to other B-doped TiO_2 powders. Therefore, 0.5 wt% of B doping was taken as the best amount of B concentration among B-doped TiO_2 powders.

Before the refinement of Zr-doped TiO_2 powders, it was assumed that dopant Zr atoms will be directly substituted by Ti atoms in TiO_2 lattice and 4 % of O lattice sites will be occupied (Chourasia and Shrivastava, 2011). Therefore, atomic position of Zr atoms which is identical to that of Ti atoms was taken as 0, 0.7500, 0.1250 with an occupancy value of 0.04. XRD patterns along with Rietveld refined data obtained according to these parameters for Zr-doped TiO_2 powders are shown in Figure 4.9. The plots of I(obs-calc) indicates that XRD patterns of the Zr-doped TiO_2 powders have fitted well to the refined data. Excluding the peak positions, I(obs-calc) plots are almost linear. The GoF values of milled TiO_2 and Zr-doped TiO_2 powders (2.58 and 2.86, respectively) are close to 1 which also indicates the good quality of fitting.

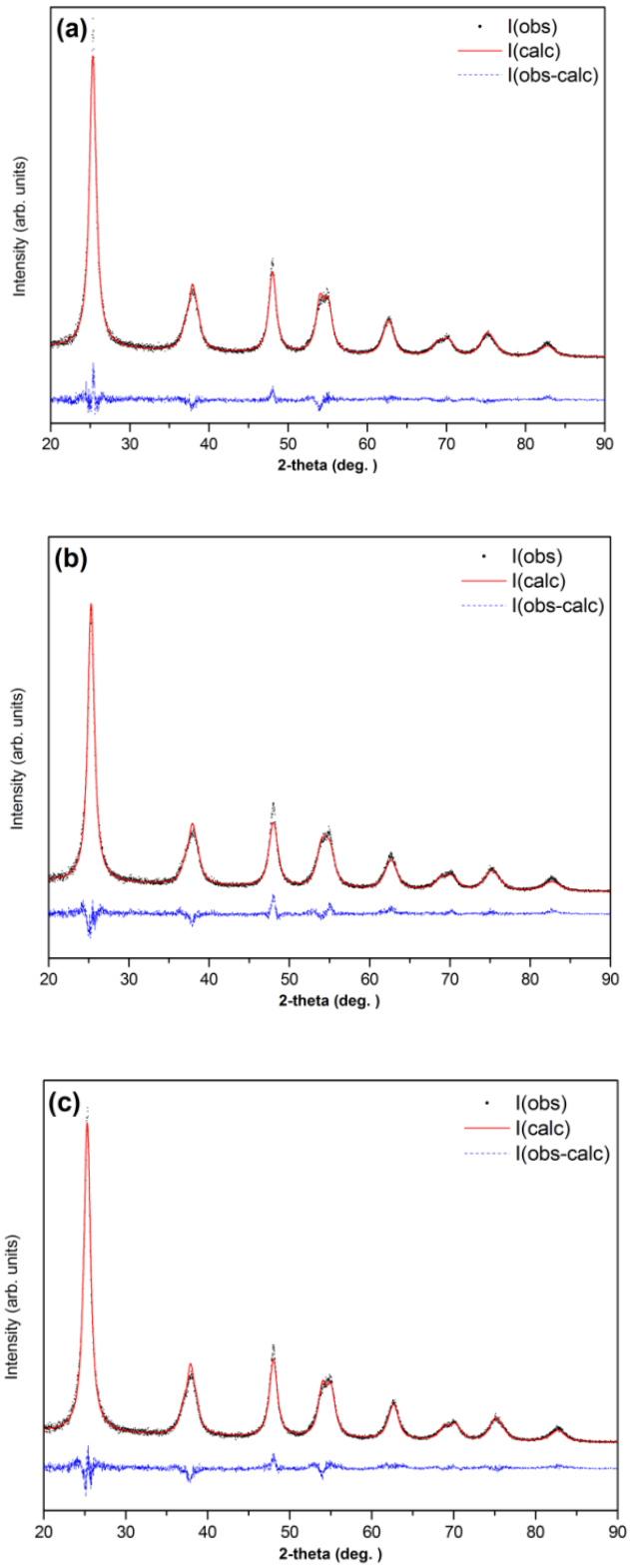

Figure 4.9. XRD patterns along with Rietveld refined data for the powders of (a) $Zr_{0.5}$-TiO_2, (b) $Zr_{1.0}$-TiO_2, and (c) $Zr_{1.5}$-TiO_2.

The values of refinement parameters obtained by Rietveld analysis for milled TiO_2 and Zr-doped TiO_2 powders are tabulated in Table 4.4.

Table 4.4. Refinement parameters of milled TiO_2 and Zr-doped TiO_2 powders.

Refinement Parameters	**Milled TiO_2**	**$Zr_{0.5}$-TiO_2**	**$Zr_{1.0}$-TiO_2**	**$Zr_{1.5}$-TiO_2**
Space group	$I4_1/amd$	$I4_1/amd$	$I4_1/amd$	$I4_1/amd$
Ti (occup.)	1.0000	0.7495	0.9608	0.9702
O (occup.)	1.0000	1.000	1.000	1.000
Zr (occup.)	-	0.1465	0.0321	0.0223
a = b (Å)*	3.7907	3.7932	3.7904	3.7902
c (Å)*	9.4838	9.4935	9.4948	9.4893
Volume ($Å^3$)	136.27	136.60	136.41	136.32
χ^2 **	8.226	6.685	7.781	7.600
Rp (%) **	7.29	6.59	7.59	7.14
Rwp (%) **	9.35	8.55	9.60	9.17

* *a,b and c are lattice parameters.*

** *$\chi 2$, Rp and Rwp are the measure of goodness of the Rietveld fitting.*

For Zr doping, only substitution mechanism is active since lattice spacing of TiO_2 is not big enough to allow Zr ions with an ionic radius of 0.084 nm to incorporate into TiO_2 crystal lattice (Reddy et al., 2009). Refined fractional atomic positions for Ti and Zr atoms are the same (0, 0.7500, 0.1250) for the milled TiO_2 and Zr-doped TiO_2 powders as seen in Table 4.5. In order to understand the doping mechanism of Zr atoms in TiO_2 lattice, fractional atomic positions of 0, 0.7500, 0.1250 for the Zr atoms were considered in Zr-doped TiO_2 powders. It has been also noted that Zr atoms remained in the same atomic positions as Zr doping to TiO_2 lattice is increased.

Table 4.5. Fractional atomic positions for milled TiO_2 and Zr-doped TiO_2 powders.

	Ti (x, y, z) 4*a*	**O (x, y, z) 8*e***	**Zr (x, y, z) 4*a***
As-received TiO_2	0, 0.7500, 0.1250	0, 0.7500, 0.3333	-
Milled TiO_2	0, 0.7500, 0.1250	0, 0.7500, 0.3333	-
$Zr_{0.5}$-TiO_2	0, 0.7500, 0.1250	0, 0.7500, 0.3333	0, 0.7500, 0.1250
$Zr_{1.0}$-TiO_2	0, 0.7500, 0.1250	0, 0.7500, 0.3333	0, 0.7500, 0.1250
$Zr_{1.5}$-TiO_2	0, 0.7500, 0.1250	0, 0.7500, 0.3333	0, 0.7500, 0.1250

The findings confirm that Zr atoms tend to enter into TiO_2 lattice via substitution of Ti atoms. Decrease in Ti occupancy value from 1.000 to lower values (0.7495 through 0.9702) is another solid proof of Zr^{4+}-Ti^{4+} substitution. Moreover, shift of diffraction peaks to smaller diffraction angles in Zr-doped TiO_2 powders, as seen in the inset of Figure 4.3, is explained by the increase in cell volume of Zr-doped powders as compared to that of as-received TiO_2 and milled TiO_2 powders. Cell volume of TiO_2 lattice increased when Zr was incorporated to the lattice because of the reason that radius of Zr^{4+} is bigger than Ti^{4+} (0.068 nm). The substitution of Ti^{4+} atoms with Zr^{4+} atoms induced lattice enlargement (Kumerasan et al., 2011). The cell volume of as-received TiO_2 powder increased from 136.27 $Å^3$ to 136.60 $Å^3$ when 0.5 wt% Zr was incorporated into TiO_2 lattice. $Zr_{0.5}$-TiO_2 powder offered the biggest cell volume among Zr-doped TiO_2 powders implying that Zr doping more than 0.5 wt% did not cause further distortion in TiO_2 lattice. This might be due to the reason that excess amount of Zr ions in milling media act as a barrier for Zr doping into TiO_2 structure by mechanical ball milling. Therefore, 0.5 wt% Zr doping was taken as the best amount of Zr concentration among Zr-doped TiO_2 powders. It has been noted that the cell volume of Zr-doped TiO_2 powders decreases as Zr doping is increased.

Data obtained from Rietveld refinement analysis were imported to a computer software program named DRAWXtl to illustrate 3-D crystal structure of Zr-doped TiO_2 powders. A typical 3-D crystal structure of $Zr_{0.5}$-TiO_2 powder is shown in Figure 4.10.

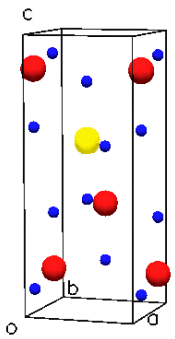

Figure 4.10. 3-D representation of the crystal structure of $Zr_{0.5}$-TiO_2 powder. Red atoms are Ti, blue atoms are O and yellow atom is Zr.

XRD patterns along with Rietveld refined data for B-Zr co-doped TiO_2 powders are shown in Figure 4.11.

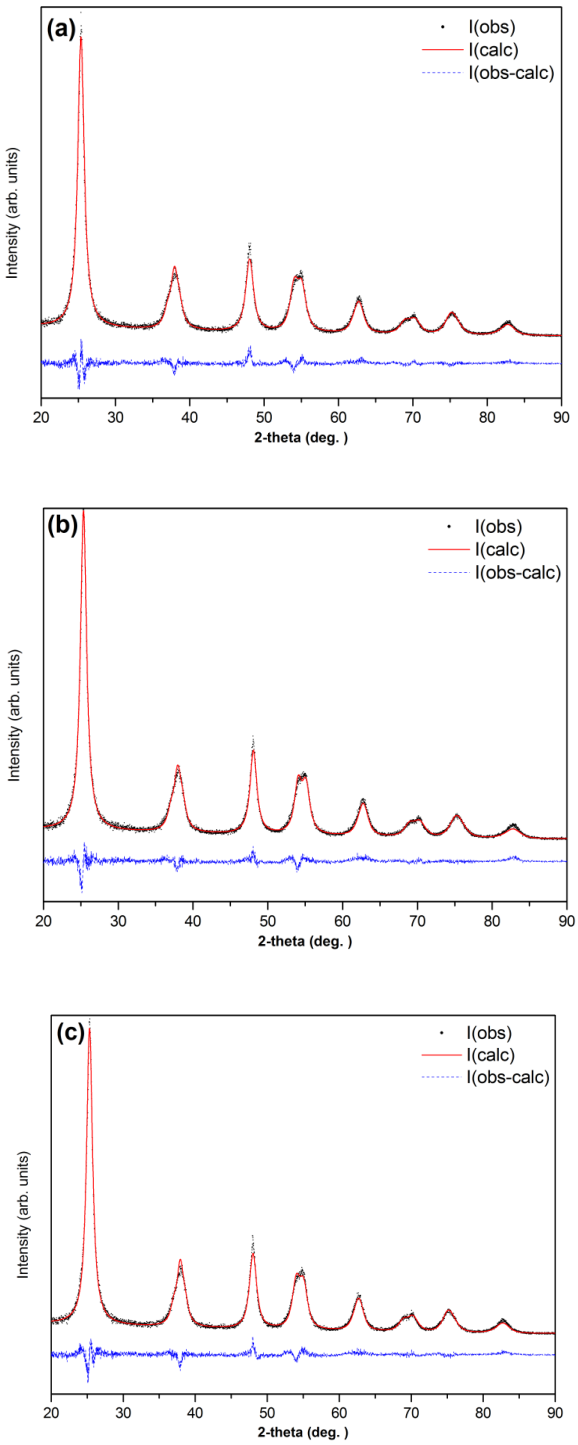

Figure 4.11. XRD pattern along with Rietveld refined data for the powders of (a) $B_{0.5}$-$Zr_{0.3}$-TiO_2, (b) $B_{0.5}$-$Zr_{0.5}$-TiO_2 and (c) $B_{0.5}$-$Zr_{0.7}$-TiO_2.

The values of refinement parameters and fractional atomic positions obtained by Rietveld analysis for milled TiO_2 and B-Zr co-doped TiO_2 powders are summarized in Tables 4.6 and 4.7, respectively.

Table 4.6. Refinement parameters of milled TiO_2 and B-Zr co-doped TiO_2 powders.

Refinement Parameters	**Milled TiO_2**	**$B_{0.5}$-$Zr_{0.3}$-TiO_2**	**$B_{0.5}$-$Zr_{0.5}$-TiO_2**	**$B_{0.5}$-$Zr_{0.7}$-TiO_2**
Space group	$I4_1/amd$	$I4_1/amd$	$I4_1/amd$	$I4_1/amd$
Ti (occup.)	1.0000	0.9369	0.9357	0.9559
O (occup.)	1.0000	1.0000	1.0000	1.0000
B (occup.)	-	0.1819	0.1138	0.0732
Zr (occup.)	-	0.0559	0.0510	0.0502
a = b (Å)*	3.7907	3.7976	3.7902	3.7901
c (Å)*	9.4838	9.4904	9.4992	9.4953
Volume ($Å^3$)	136.27	136.87	136.46	136.40
χ^2 **	8.226	7.245	7.724	7.533
Rp (%) **	7.29	6.90	6.82	6.85
Rwp (%) **	9.35	8.74	8.83	8.75

* *a,b and c are lattice parameters.*

** *$\chi 2$, Rp and Rwp are the measure of goodness of the Rietveld fitting.*

Table 4.7. Fractional atomic positions of milled TiO_2 and B-Zr co-doped TiO_2 powders.

	Ti (x, y, z) 4*a*	**O (x, y, z) 8*e***	**B (x, y, z) 8*e***	**Zr (x, y, z) 4*a***
As-received TiO_2	0, 0.7500, 0.1250	0, 0.7500, 0.3333	-	-
Milled TiO_2	0, 0.7500, 0.1250	0, 0.7500, 0.3333	-	-
$B_{0.5}$-$Zr_{0.3}$-TiO_2	0, 0.7500, 0.1250	0, 0.7500, 0.3333	0, 0.7500, 0.2987	0, 0.7500, 0.1250
$B_{0.5}$-$Zr_{0.5}$-TiO_2	0, 0.7500, 0.1250	0, 0.7500, 0.3333	0, 0.7500, 0.2944	0, 0.7500, 0.1250
$B_{0.5}$-$Zr_{0.7}$-TiO_2	0, 0.7500, 0.1250	0, 0.7500, 0.3333	0, 0.7500, 0.2955	0, 0.7500, 0.1250

All Rietveld refinement analysis results including occupancy of atoms and fractional atomic positions for B-Zr co-doped TiO_2 powders are in consistent with Rietveld refinement analysis results for only B or only Zr doped TiO_2 powders.

In B-Zr co-doped TiO_2 powders, B and Zr atoms present in TiO_2 lattice have different atomic positions than Ti and O atoms as seen in Table 4.6. Refined values of cell volume in B-Zr co-doped TiO_2 powders confirm that incorporation of B and Zr ions into TiO_2 lattice gives rise to additional distortion and increase in cell volume. Also, the shift of diffraction peaks to smaller diffraction angles in B-Zr co-doped TiO_2 powders as compared to milled TiO_2 powders, as seen in the inset of Figure 4.4, is explained by increase in cell volume of B-Zr co-doped powders. The highest distortion in TiO_2 lattice was obtained by 0.5 wt% B and 0.3 wt% Zr co-doping. A comparison of cell volume (136.27 $Å^3$) of milled TiO_2 powder with that of $B_{0.5}$-$Zr_{0.3}$-TiO_2, $B_{0.5}$-$Zr_{0.5}$-TiO_2, and $B_{0.5}$-$Zr_{0.7}$-TiO_2 powders (136.87, 136.46, and 136.40 $Å^3$, respectively) verifies that synergistic effect of interstitial B doping and substitutional Zr doping has made a bigger impact in terms of increase in cell volume as compared to milled TiO_2, as well as B-doped TiO_2, and Zr-doped TiO_2 powders. This result signifies that B-Zr co-doping causes further distortion in TiO_2 lattice. $B_{0.5}$-$Zr_{0.3}$-TiO_2 powder offered the biggest cell volume among B-Zr co-doped TiO_2 powders.

Data obtained from Rietveld refinement analysis were imported to a computer software program named DRAWXtl to illustrate 3-D crystal structure of B-Zr-doped TiO_2 powders. A typical 3-D crystal structure of $Zr_{0.5}$-TiO_2 powder is shown in Figure 4.12.

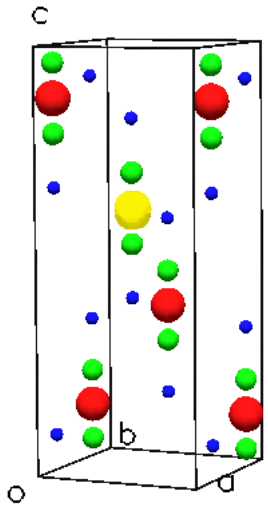

Figure 4.12. 3-D representation of the crystal structure of $B_{0.5}$-$Zr_{0.3}$-TiO_2 powder. Red atoms are Ti, blue atoms are O and yellow atom is Zr

Rietveld refinement analysis also makes it possible to calculate the crystallite size of powders accurately from their X-ray diffraction pattern. During the analysis, a lorentzian coefficient named "LX" which is concerned with broadening of the peaks, is refined and by

employing the formula given below, exact value of crystallite size is obtained (Larson and Von Dreele, 2004);

$$C = \frac{18000K\lambda}{\pi(LX)}$$

where; C represents the crystallite size. λ is the wavelength of the X-ray source used which is 1.5418 in this study. K is the Scherrer constant taken as 0.9 for spherical shaped particles (Maurya and Chauhan, 2011).

As mentioned previously, all of the TiO_2 powders investigated except as-received TiO_2 were ball milled. Thus reduction in their particle size as compared to initial particle size is expected. Crystallite size values as calculated by Rietveld refinement analysis as well as particle size values as calculated by SEM micrographs for all of the powders investigated are listed in Table 4.8.

Table 4.8. Crsytallite and particle size values as calculated by Rietveld refinement analysis and SEM analysis, respectively.

Powder	**Crystallite size (nm)**	**Particle size (nm)**
As-received TiO_2	32.2	105.6
Milled TiO_2	8.6	26.7
$B_{0.5}$-TiO_2	7.6	27.8
$B_{1.0}$-TiO_2	7.9	27.2
$B_{1.5}$-TiO_2	8.5	26.9
$Zr_{0.5}$-TiO_2	8.1	33.5
$Zr_{1.0}$-TiO_2	8.6	30.6
$Zr_{1.5}$-TiO_2	8.7	29.3
$B_{0.5}$-$Zr_{0.3}$-TiO_2	8.0	36.6
$B_{0.5}$-$Zr_{0.5}$-TiO_2	8.2	32.4
$B_{0.5}$-$Zr_{0.7}$-TiO_2	8.5	30.7

As seen in Table 4.8, crystallite size of all TiO_2 powders are very close to each other and less than 10 nm except as-received TiO_2 powder. The manufacturer of as-received TiO_2 powder quotes particle size of this powder as less than 1 μm. Crystallite size of as-received TiO_2 powder as calculated by Rietveld refinement analysis was much lower (nearly 30 nm) than 1 μm. The difference between quoted and calculated values of particle size in this powder is due to first the difference of measurement techniques. Quoted values have been measured by a particle size analyser. It is envisaged that the particles are agglomerated during the measurement. Second, crystallite size calculated by Rietveld refinement analysis reports the size of the small crystals which held together to constitute a polycrystalline TiO_2 powder whereas particle size measured by particle size analyser reports the size of primary, secondary particles and agglomerated particles. Therefore, powders having larger

particle size than crystallite size are an expected result. Nonetheless, as understood from the difference in particle size between as-received and milled and/or doped/co-doped powders, it is evident that ball milling reduced the particle size of as-received TiO_2 powder.

4.2.2 X-ray Photoelectron Spectroscopy (XPS)

Broad scan XPS spectrum of $B_{0.5}$-$Zr_{0.3}$-TiO_2 powder is shown in Figure 4.13. B and Zr, originated from the dopants during the milling process, are detected in the spectrum. The occurrence of B and Zr may be due to the two reasons; dopant B and Zr atoms are chemically bonded with lattice Ti and O atoms or doped into the TiO_2 lattice structure. Which one of these reasons is valid could be realized after analysing detailed XPS scans recorded for B 1s, Zr 3d and Ti 2p.

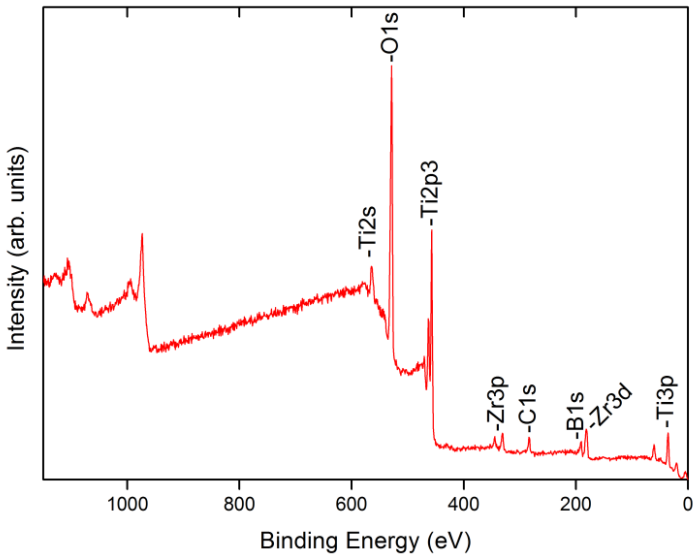

Figure 4.13. Broad scan XPS spectrum of $B_{0.5}$-$Zr_{0.3}$-TiO_2 powder.

XPS spectrum of $B_{0.5}$-$Zr_{0.3}$-TiO_2 powder for B 1s is shown in Figure 4.14. A pseudo-Voigt peak shape function was used for peak fitting and the binding energy (BE) for B 1s was determined as 191.8 eV. It has been reported that BE for B 1s is 193.6 eV in B_2O_3 (Joyner and Hercules, 1980), 193.0 eV in H_3BO_3 (Schreifels et al., 1980), and 187.5 eV in TiB_2 (Mavel et al., 1973). The XPS results verify that the B atoms are not bonded to either Ti or O atoms by means of B-Ti-B or B-O-B bonds.

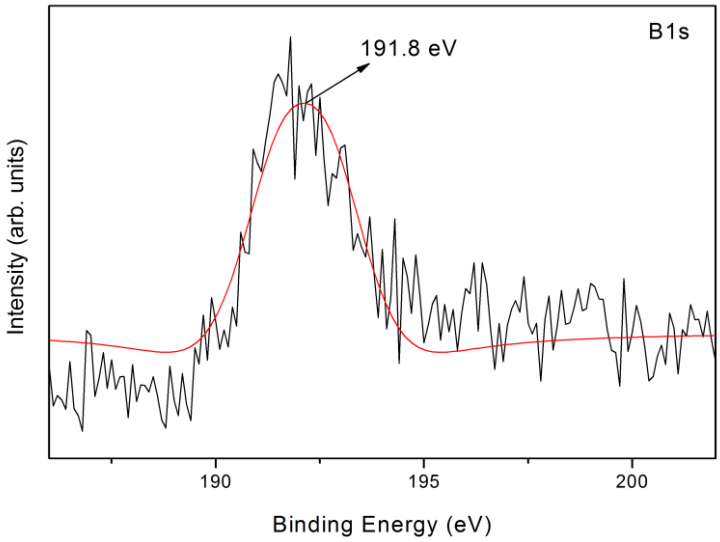

Figure 4.14. XPS spectra of $B_{0.5}$-$Zr_{0.3}$-TiO_2 powder for B 1s.

XPS spectrum of $B_{0.5}$-$Zr_{0.3}$-TiO_2 powder for Ti 2p is shown in Figure 4.15. BEs for Ti 2p are 458.0 eV and 463.6 eV which are attributed to Ti $2p_{3/2}$ and Ti $2p_{1/2}$ of TiO_2, respectively. BE for Ti $2p_{3/2}$ is 454.4 eV in TiB_2 (Mavel et al., 1973) which clarifies that neither the compound TiB_2 nor the B-Ti bond is existent in $B_{0.5}$-$Zr_{0.3}$-TiO_2 powder.

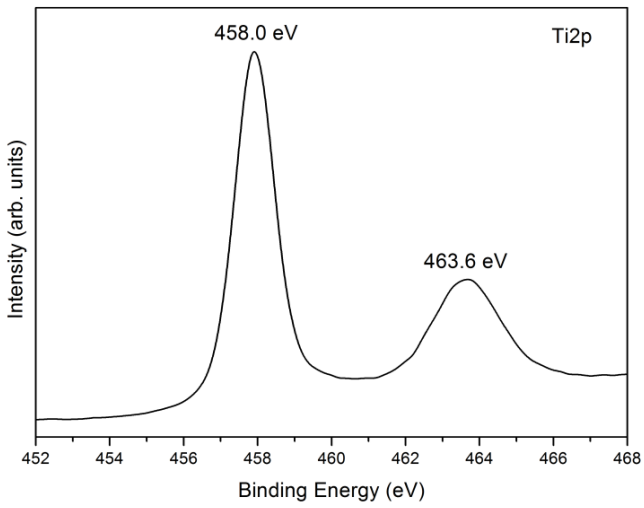

Figure 4.15. XPS spectra of $B_{0.5}$-$Zr_{0.3}$-TiO_2 powder for Ti 2p.

XPS spectrum of $B_{0.5}$-$Zr_{0.3}$-TiO_2 powder for Zr 3d is shown in Figure 4.16. Again a pseudo-Voigt peak shape function was used for peak fitting and the BEs for Zr 3d were 181.6 eV and 184.0 eV. BE for Zr 3d was 179.4 eV in ZrH_x, 179.96 eV in Zr_2O, 180.64 eV in ZrO, 182.03 eV in Zr_2O_3, and 183.10 eV in ZrO_2 (Bastl et al., 2002). Results make clear that the Zr-O and

Zr-H bonds hence the compounds of ZrH_x and Zr_xO_y are not present in $B_{0.5}$-$Zr_{0.3}$-TiO_2 powder.

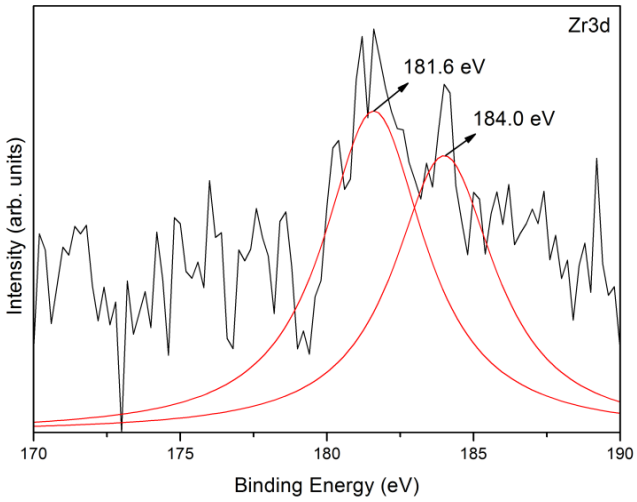

Figure 4.16. XPS spectra of $B_{0.5}$-$Zr_{0.3}$-TiO_2 powder for Zr 3d.

The existence of B and Zr in broad scan XPS spectra and detection of no new compound between B, Zr, O, and Ti atoms other than TiO_2, clearly ascertain that B and Zr atoms doped into TiO_2 crystal lattice.

4.2.3 Scanning Electron Microscope (SEM) and Energy Dispersive Spectroscopy (EDS)

Surface morphologies of as-received TiO_2, milled $TiO_2.H_2O$, and milled TiO_2 powders are shown in SEM images in Figure 4.17. SEM investigation revealed that these powders consisted of irregularly shaped, agglomerated particles. The surface morphology and shape of the particles did not change after ball milling.

Particle size of the powders as determined from SEM images by using a computer software program named ImageJ are given in Table 4.8. It is worthy to note that these results are not precise and do not represent the average particle size of the powders since the particles are highly agglomerated. The agglomeration of particles is attributed to the mechanical energy that accelerated the aggregation since the fresh surfaces exposed by the milling lowers their high surface energy by agglomeration (Hennart et al., 2012). Particle size data in Table 4.8 indicate that particle size of as-received powder is 105.6 nm which is about three times larger than the crystallite size (32.24 nm) calculated by Rietveld analysis for this powder. However, particle size of the powders has been measured for comparison of the size of particles before and after ball milling and after B and/or Zr doping. As expected, particle size of as-received TiO_2 powder decreased after ball milling since ball milling process causes particle size refinement (Suryanarayana, 2001). After ball milling, particle size of as-received TiO_2 powder decreased from 105.6 nm to 25.3 nm. However, particle size of the powder increased for a few nanometers after calcination process due to the tendency of particles to grow and get agglomerated by the effect of heat

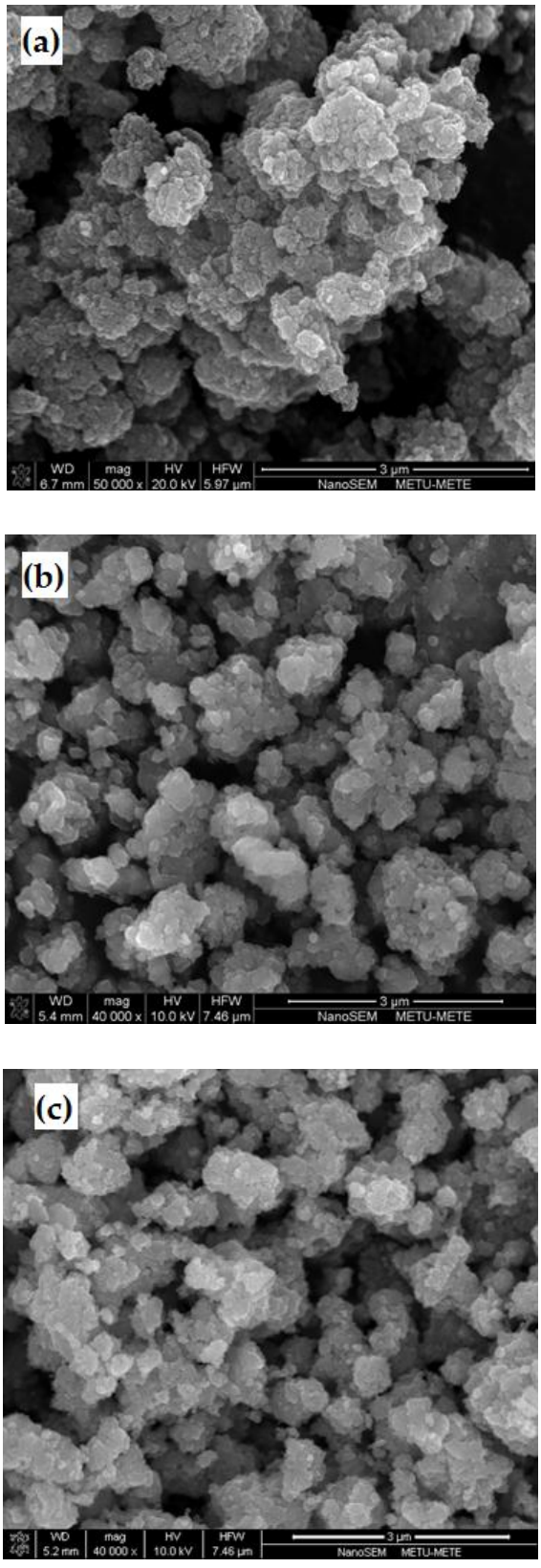

Figure 4.17. SEM images for the powders of (a) as-received TiO_2, (b) milled $TiO_2.H_2O$, and (c) milled TiO_2.

Elemental composition as determined by EDS analysis for as-received TiO_2, milled $TiO_2.H_2O$, and milled TiO_2 powders are given in Table 4.9. As expected, elemental compositions (O and Ti concentrations) of these powders are almost the same and proper to empirical formula of TiO_2.

Table 4.9. Elemental composition for as-received TiO_2, milled $TiO_2.H_2O$, and milled TiO_2 powders.

	As-received TiO_2	**Milled $TiO_2.H_2O$**	**Milled TiO_2**
Element	wt%	wt%	wt%
O K	44.82	44.60	41.17
Ti K	55.18	55.40	58.83

Surface morphologies of $B_{0.5}$-TiO_2, $B_{1.0}$-TiO_2, and $B_{1.5}$-TiO_2 powders are shown in SEM images in Figure 4.18. SEM investigation revealed that B-doped TiO_2 powders are consisted of irregularly shaped, agglomerated particles. The surface morphology and shape of the particles did not change when dopant B concentration is increased.

Particle size of the powders as determined from SEM images by using the computer software program are given in Table 4.8. Particle size of $B_{0.5}$-TiO_2 powder is 28.7 nm which is about three times larger than the crystallite size (7.56 nm) calculated by Rietveld analysis for this powder as seen in Table 4.8. Moreover, the particle size is a few nanometers larger than that (26.7 nm) of milled TiO_2 powder might be due to the increase in cell volume. Since $B_{0.5}$-TiO_2 has a larger cell volume (136.48 $Å^3$) than milled TiO_2 powder (136.27 $Å^3$) due to incorporation of interstitial B atoms into TiO_2 lattice, an increase in particle size is expected. Also, particle size of $B_{0.5}$-TiO_2 powder decreased from 28.7 nm to 25.5 nm for $B_{1.0}$-TiO_2 powder and to 21.4 nm for $B_{1.5}$-TiO_2 powder. It is obvious that the particle size decreases due to reduction of cell volume with increasing B concentration as discussed in Section 4.1.

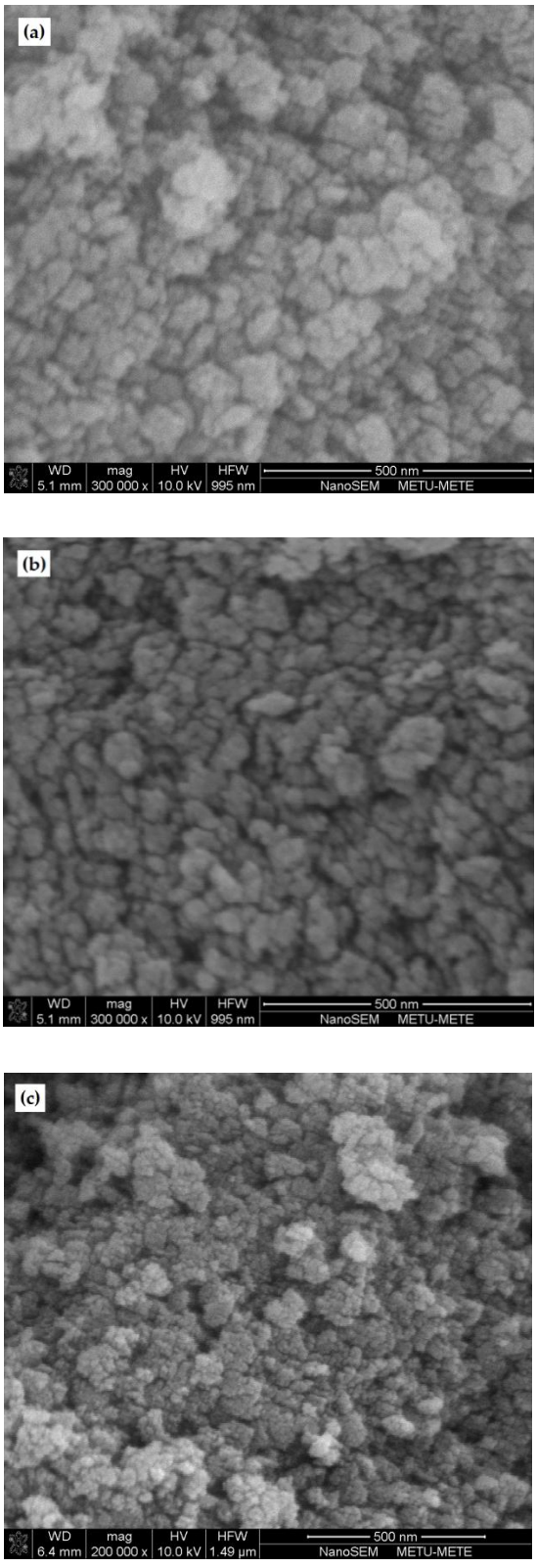

Figure 4.18. SEM images for powders of (a) $B_{0.5}$-TiO_2, (b) $B_{1.0}$-TiO_2, and (c) $B_{1.5}$-TiO_2.

Elemental composition as determined by EDS analysis for the B-doped TiO_2 powders are given in Table 4.10. As expected, B concentration in B-doped powders increases as the amount of H_3BO_3 solution added to as-received powder during ball milling is increased. Since there is no substitution mechanism between B and Ti atoms, Ti concentration of the B-doped powders remained almost the same when dopant B concentration is increased. Moreover, all the compositions present in the B-doped TiO_2 powders are proper to empirical formula of TiO_2.

Table 4.10. Elemental composition of the B-doped TiO_2 powders.

	$B_{0.5}$-TiO_2	**$B_{1.0}$-TiO_2**	**$B_{1.5}$-TiO_2**
Element	wt%	wt%	wt%
O K	43.26	42.43	42.16
Ti K	56.30	56.60	56.52
B K	0.44	0.97	1.32

Surface morphologies of the Zr-doped TiO_2 powders are shown in SEM images in Figure 4.19. SEM investigation revealed that the Zr-doped TiO_2 powders are consisted of irregularly shaped and agglomerated particles, too. The surface morphology and shape of the particles did not change when dopant Zr concentration is increased.

Particle size of the powders as determined from SEM images by using the computer software program are given in Table 4.8. Particle size of $Zr_{0.5}$-TiO_2 powder is 33.5 nm which is about three times larger than the crystallite size (8.11 nm) calculated by Rietveld analysis for this powder as seen in Table 4.8. Particle size of $Zr_{0.5}$-TiO_2 powder is a few nanometer larger than that (26.7 nm) of milled TiO_2 powder. Since substitution of Zr atoms with Ti atoms in TiO_2 lattice results in a larger cell volume (136.60 $Å^3$) as compared with cell volume of milled TiO_2 (136.27 $Å^3$), an increase in particle size is expected. Also, particle size of $Zr_{0.5}$-TiO_2 powder decreased from 33.5 nm to 30.6 nm for $Zr_{1.0}$-TiO_2 powder and to 29.3 nm for $Zr_{1.5}$-TiO_2 powder. It is obvious that the particle size decreases due to reduction of cell volume with increasing Zr concentration as discussed in Section 4.1.

When a comparison is made between the particle size of the Zr-doped TiO_2 powders and that of the B-doped TiO_2 powders, correlation between cell volume and particle size of the powders is further clarified. As substitutional Zr atoms are more effective in increasing cell volume of TiO_2 lattice than interstitial B atoms as discussed in Section 4.1. Particle size determination from SEM images confirmed that particle size of Zr-doped TiO_2 powders (29.3 nm through 33.5 nm) are a few nanometers larger than that of B-doped TiO_2 powders (26.9 nm through 27.8 nm).

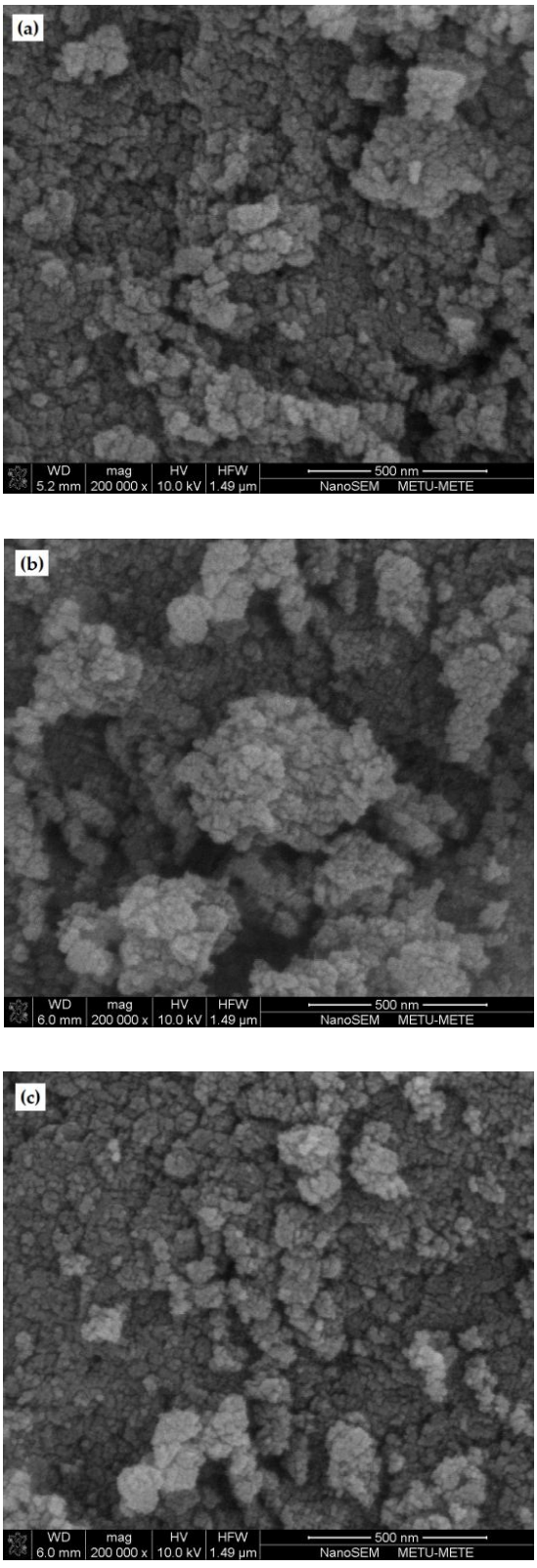

Figure 4.19. SEM images for powders of (a) $Zr_{0.5}$-TiO_2, (b) $Zr_{1.0}$-TiO_2, and (c) $Zr_{1.5}$-TiO_2.

Elemental composition as determined by EDS analysis for the Zr-doped TiO_2 powders are given in Table 4.11. As expected, Zr concentration in Zr-doped powders increases as the amount of $Zr(C_5H_7O_2)_3$ solution added to as-received powder during ball milling is increased. Since there is a substitution mechanism between Zr and Ti atoms, Ti concentration of the Zr-doped powders decreased as dopant Zr concentration was increased. Moreover, all the compositions present in the Zr-doped powders are proper to empirical formula of TiO_2.

Table 4.11. Elemental composition of the Zr-doped TiO_2 powders.

	$Zr_{0.5}$-TiO_2	**$Zr_{1.0}$-TiO_2**	**$Zr_{1.5}$-TiO_2**
Element	wt%	wt%	wt%
O K	42.80	42.98	43.01
Ti K	56.88	56.16	55.44
Zr K	0.32	0.86	1.55

Surface morphologies of B-Zr co-doped TiO_2 powders are shown in SEM images in Figure 4.20. SEM examination revealed that the B-Zr co-doped TiO_2 powders are consisted of irregularly shaped and agglomerated particles, too. The surface morphology and shape of the particles did not change when dopants B and Zr concentrations are increased.

Particle size of the powders was determined from SEM images by using a computer software program named ImageJ. The results are given in Table 4.8. Particle size of $B_{0.5}$-$Zr_{0.3}$-TiO_2 powder is 36.6 nm which is about three times larger than the crystallite size (8.00 nm) calculated by Rietveld analysis for this powder as seen in Table 4.8. Particle size of $B_{0.5}$-$Zr_{0.3}$-TiO_2 powder is a few nanometers larger than that (26.7 nm) of milled TiO_2 powder. Since interstitial B and substitutional Zr atoms in TiO_2 lattice results in a larger cell volume (136.87 $Å^3$) as compared with cell volume of milled TiO_2 (136.27 $Å^3$), an increase in particle size is expected. Also, particle size of $B_{0.5}$-$Zr_{0.3}$-TiO_2 powder decreased from 36.6 nm to 32.4 nm for $B_{0.5}$-$Zr_{0.5}$-TiO_2 powder and to 30.7 nm for $B_{0.5}$-$Zr_{0.7}$-TiO_2 powder. It is obvious that the particle size decreases due to reduction of cell volume with increasing Zr concentration as discussed in Section 4.1.

It is observed that as the amount of Zr doping increases, the particle size decreases for a few nanometers due to reduction of cell volumes with increasing Zr content as discussed in Section 4.1. When a comparison is made between the particle sizes of the B-Zr co-doped TiO_2 powders and that of the B-doped and Zr-doped TiO_2 powders, synergistic effect of B-Zr co-doping on increase in cell volume of TiO_2 lattice results in the largest particle size of $B_{0.5}$-$Zr_{0.3}$-TiO_2 powder (36.6 nm) among other powders (33.5 nm through 26.9 nm).

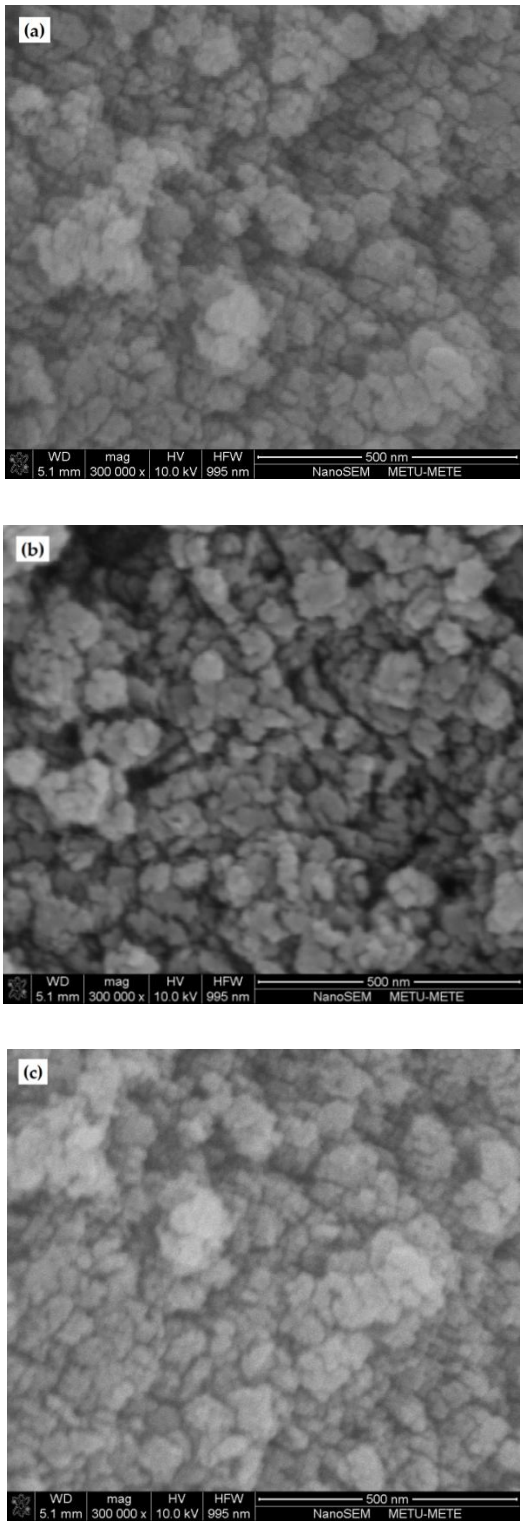

Figure 4.20. SEM images for powders of (a) $B_{0.5}$-$Zr_{0.3}$-TiO_2, (b) $B_{0.5}$-$Zr_{0.5}$-TiO_2, and (c) $B_{0.5}$-$Zr_{0.7}$-TiO_2.

Elemental composition as determined by EDS analysis for the B-Zr co-doped TiO_2 powders are given in Table 4.12. As expected, Zr concentration in B-Zr co-doped powders increases

as the amount of Zr addition is increased. Since there is a substitution mechanism between Zr and Ti atoms, Ti content of the B-Zr co-doped powders decreased as Zr content of the powders increased. Moreover, all the compositions present in the B-Zr co-doped powders are close to empirical formula of TiO_2.

Table 4.12. Elemental composition of the B-Zr co-doped TiO_2 powders.

	$B_{0.5}$-$Zr_{0.3}$-TiO_2	**$B_{0.5}$-$Zr_{0.5}$-TiO_2**	**$B_{0.5}$-$Zr_{0.7}$-TiO_2**
Element	wt%	wt%	wt%
O K	43.25	43.38	43.53
Ti K	56.20	55.77	55.34
B K	0.44	0.46	0.52
Zr K	0.11	0.39	0.61

4.3 PHOTOCATALYTIC ACTIVITY

The absorbance spectra obtained after UV illumination for all of the powders investigated are given in Figure 4.21. The absorbance spectrum for the methylene blue (MB) solution was included in the figure for comparison purposes.

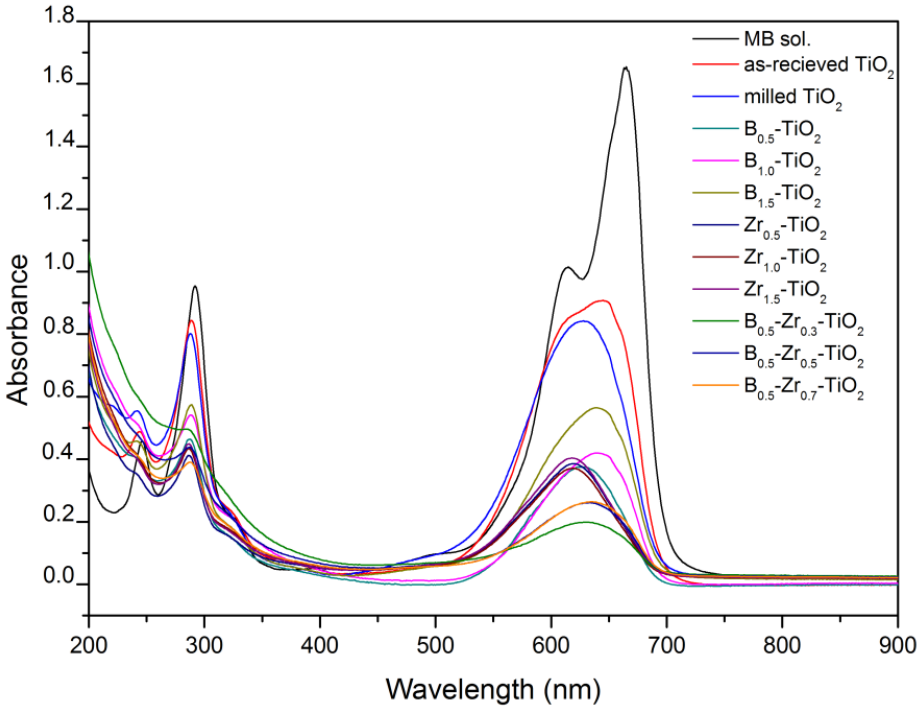

Figure 4.21. Absorbance spectra for all of the powders investigated.

The degradation of MB solution with time in dark and in UV illumination for as-received TiO_2, milled $TiO_2.H_2O$, and milled TiO_2 powders are shown in Figure 4.23. The results of MB degradation occurred for all of the powders investigated are presented in Table 4.13. It is apparent that all powders are active in the reaction of photocatalytic degradation of MB in UV light as well as in dark which implies that as-received TiO_2 powder has a significant amount of adsorption capacity for MB (Nguyen-Phan et al., 2011). Main reasons of this adsorption capacity are related to porous structure of as-received TiO_2 powder with large specific surface area and OH^- groups on the surface of TiO_2 powder (Rouquérol et al., 1999; Liu et al., 2012). Figure 4.22 shows the adsorption of MB on a (001) surface of TiO_2. The MB molecules adhere to the surface OH^- radicals of TiO_2 which is responsible for instantaneous increase in photocatalytic activity in dark.

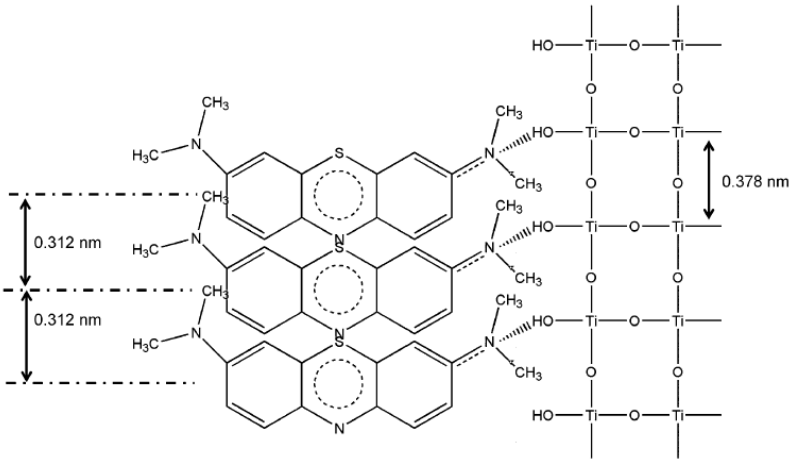

Figure 4.22. Adsorption of MB molecules on a (001) surface of TiO_2 (Liu et al., 2012).

Adsorption kinetics related with size of the adsorbent pores and dimensions of the diffusing adsorbate molecules (Nguyen et al., 2012). As the MB molecule could be assumed to have a volume of (0.42 nm^3) (Pham and Brindley, 1970), TiO_2 powder with an average pore diameter about 2-5 nm can easily trap multiple molecules of MB within the pores. From the SEM figures in Section 4.2.3, it is clear that prepared TiO_2 powder particles consists of many nanosized pores (2-5 nm), which explains the adsorption mechanism of MB by TiO_2 particles in this study. When the powders were kept in dark for 30 min, as-received TiO_2 decomposed only 39.2% of MB whereas MB decomposition by milled $TiO_2.H_2O$ and milled TiO_2 powders was 45.2% and 46.7%, respectively. MB adsorption capacity of as-received TiO_2 increased by the milling process which caused particle refinement hence provided larger surface area for the milled powders. Since a higher surface area provided more space for the penetration of MB, superior MB decomposition of milled $TiO_2.H_2O$ powder as compared to as-received TiO_2 powder is expected (Nguyen et al., 2012). Approximately 6% improvement in photocatalytic efficiency was achieved by the milling process. It is noted that milled TiO_2 powder has approximately 1% additional improvement in photocatalytic efficiency due to the calcination process as compared to milled $TiO_2.H_2O$ powder. The improvement in photocatalytic efficiency caused by calcination is due to the further anatase crystallization and the smoothening of particle surface so that MB could easily penetrate into the milled TiO_2 powder.

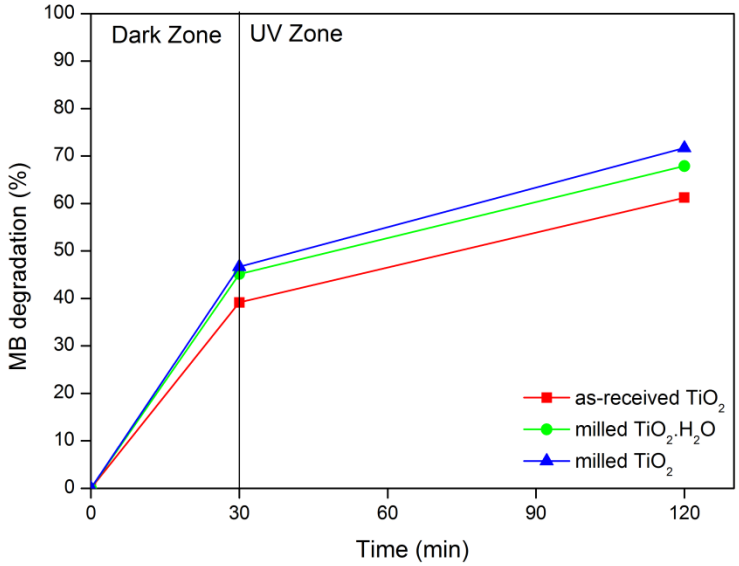

Figure 4.23. MB degradation with time in dark and in UV illumination for as-received TiO_2, milled $TiO_2.H_2O$, and milled TiO_2 powders.

Table 4.13. MB degradation percentages for all of the powders investigated.

Powder	MB Degradation (%)	
	30 min in dark	30 min in dark followed by 90 min in UV
as-received TiO_2	39.2	61.3
milled $TiO_2.H_2O$	45.2	67.9
milled TiO_2	46.7	71.7
$B_{0.5}$-TiO_2	66.1	88.5
$B_{1.0}$-TiO_2	55.8	82.5
$B_{1.5}$-TiO_2	50.1	74.1
$Zr_{0.5}$-TiO_2	49.2	90.3
$Zr_{1.0}$-TiO_2	48.1	89.5
$Zr_{1.5}$-TiO_2	47.3	88.7
$B_{0.5}$-$Zr_{0.3}$-TiO_2	75.2	91.7
$B_{0.5}$-$Zr_{0.5}$-TiO_2	75.1	88.2
$B_{0.5}$-$Zr_{0.7}$-TiO_2	74.6	86.3

After exposing the powders to UV illumination for 90 min, total degradation of MB occurred in as-received TiO_2, milled $TiO_2.H_2O$, and milled TiO_2 powders were 61.3%, 67.9%, and 71.7%, respectively. Photocatalytic activity of as-received TiO_2 increased by the milling process which caused particle refinement hence provided larger surface area for the milled powders. Since the photocatalysis reactions take place on the surface of photocatalyst (Parrino et al., 2012), superior MB decomposition of milled $TiO_2.H_2O$ powder as compared to as-received TiO_2 powder is expected. In UV light, approximately 5% improvement in photocatalytic efficiency was achieved by the milling process. It is noted

that milled TiO_2 powder has approximately 5% additional improvement in photocatalytic efficiency due to the calcination process as compared to milled $TiO_2.H_2O$ powder.

The photocatalytic degradation of MB in the presence of TiO_2 powders could be described by first-order kinetic mechanism as (Park, 2010):

$$\ln \frac{C0}{Ct} = k_{ap}t$$

Where k_{ap} is apparent rate constant, and C0 and Ct are the concentration of MB at initial time and at time *t*, respectively. As seen in Figure 4.21, the MB degradation in UV illumination was more than that in dark for these powders, though the rate was lower due to decreased MB concentration in the solution. The MB degradation rate with time is separately shown in Figure 4.24. Since adsorption of MB took place instantaneously within 10 min, photocatalytic degradation of MB in the presence of UV illumination is assumed to be slower than adsorption process (Al-Ghouti et al., 2009).

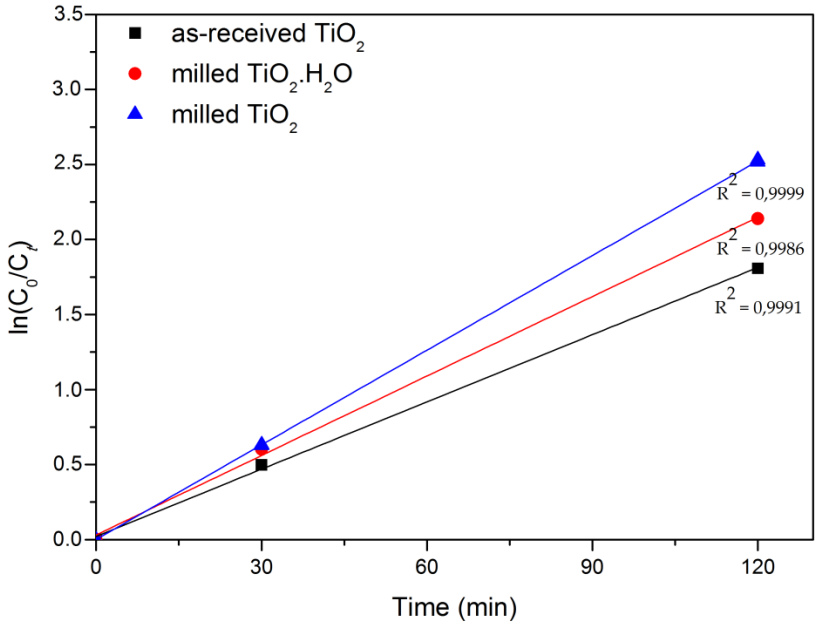

Figure 4.24. The variation of $\ln(C_0/C_t)$ with time for as-received TiO_2, milled $TiO_2.H_2O$, and milled TiO_2 powders.

Since all of the doped and co-doped powders were calcined after milling, milled TiO_2 powder was taken as reference powder in order to explain the effect of B and/or Zr doping/co-doping on the photocatalytic activity of TiO_2 powders.

The degradation of MB solution with time in dark and in UV illumination for reference TiO_2 powder and the B-doped TiO_2 powders is shown in Figure 4.25. The values of MB degradation occurred in these powders are presented in Table 4.13. It is obvious that all powders are active in the reaction of photocatalytic degradation of MB in UV illumination

as well as in dark. When the powders were kept in dark for 30 min, milled TiO_2 powder decomposed only 46.7% of MB whereas $B_{0.5}$-TiO_2, $B_{1.0}$-TiO_2, and $B_{1.5}$-TiO_2 powders decomposed 66.1%, 55.8%, and 50.1% of MB, respectively. In dark, approximately 20% improvement in MB decomposition was achieved by 0.5% B doping to TiO_2. Further increase in B doping did not improve the photocatalytic efficiency of the B-doped TiO_2 powders. The improvement in MB decomposition as compared to milled TiO_2 powder was 9% and 3% of MB for $B_{1.0}$-TiO_2 and $B_{1.5}$-TiO_2 powders, respectively.

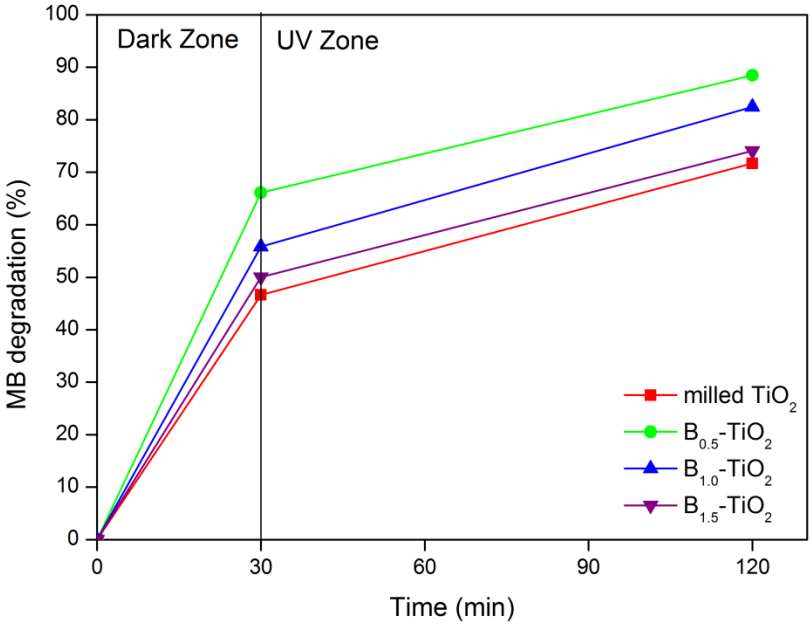

Figure 4.25. MB degradation with time in dark and in UV illumination for milled TiO_2 powder and the B-doped TiO_2 powders.

After exposing the powders to UV illumination for 90 min, total degradation of MB occurred for $B_{0.5}$-TiO_2, $B_{1.0}$-TiO_2, and $B_{1.5}$-TiO_2 powders were 88.5%, 82.5%, and 74.1%, respectively. It is clear that the MB degradation in UV illumination was more than that in dark for these powders, though the rate was lower. The MB degradation rate with time for these powders is separately shown in Figure 4.26.

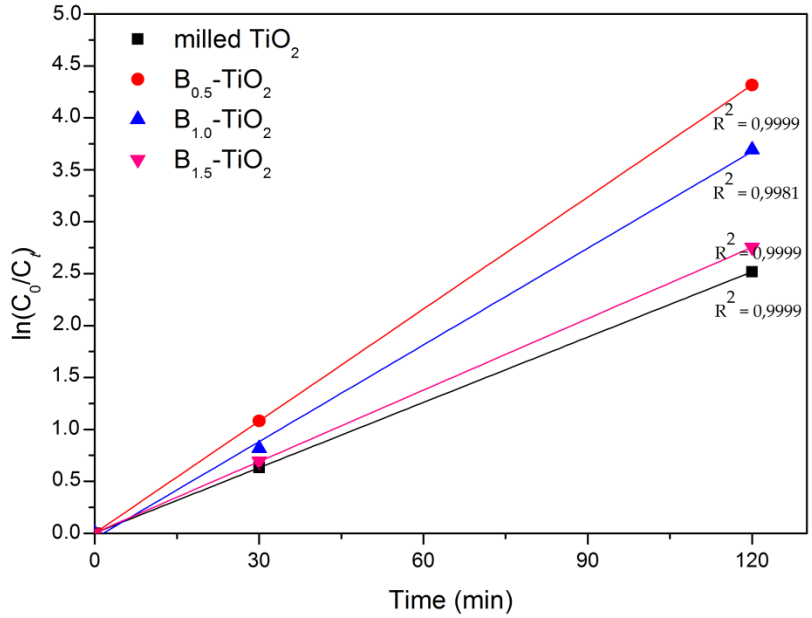

Figure 4.26. The variation of $\ln(C_0/C_t)$ with time for milled TiO_2 powder and the B-doped TiO_2 powders.

Small amount (0.5 wt%) of B doping improved the photocatalytic efficiency of milled TiO_2 powder. The MB degradation in UV illumination for $B_{0.5}$-TiO_2 powder (88.5%) was better than that for milled TiO_2 powder (71.7%) due to the narrowing of the band gap of TiO_2. After doping TiO_2 with B, the interstitial B atoms in TiO_2 lattice narrowed the band gap and increased the optical absorption of TiO_2 (Yuan et al., 2011). The photocatalytic mechanism of B-doped TiO_2 powders is illustrated schematically in Figure 4.27. In the schematic illustration, photo generated electrons transferred from valence band to conduction band of undoped TiO_2 under UV illumination (process A). In B-doped TiO_2, electrons can be excited simultaneously from the B1s energy level to conduction band (process B) which leads to intensification in photocatalytic efficiency by ~3-17% in the B-doped TiO_2 powders as compared to undoped TiO_2 powder. Also, the adsorption of MB in dark depends on the interaction between π-electrons of MB ring and surface OH groups. Since there are many OH groups on the surface of TiO_2, oxidation states of Ti and O and thus, oxidation activity of TiO_2 powder could be increased by dopant B atoms which leads to improvement in adsorption capacity in the dark (Nguyen et al., 2012).

Among the B-doped TiO_2 powders, $B_{0.5}$-TiO_2 powder offered the best individual photocatalytic efficiency in dark and in UV illumination. Further increase in B doping did not improve the photocatalytic efficiency of $B_{0.5}$-TiO_2 powder even in UV illumination. This is attributed to the amount of B ions present in the TiO_2 lattice. Rietveld analysis results in Section 4.1 revealed that more atomic sites of B in TiO_2 lattice were occupied in $B_{0.5}$-TiO_2 powder than $B_{1.0}$-TiO_2 and $B_{1.5}$-TiO_2 powders, implying that more B ions were incorporated into the TiO_2 lattice in $B_{0.5}$-TiO_2 powder. Therefore, it is anticipated that the band gap narrowing effect was more active in $B_{0.5}$-TiO_2 powder than in $B_{1.0}$-TiO_2 and $B_{1.5}$-TiO_2 powders. Conclusively, 0.5 wt% of B doping was taken as the best amount of B

concentration among the B-doped TiO_2 powders in terms of the improvement in the photocatalytic efficiency.

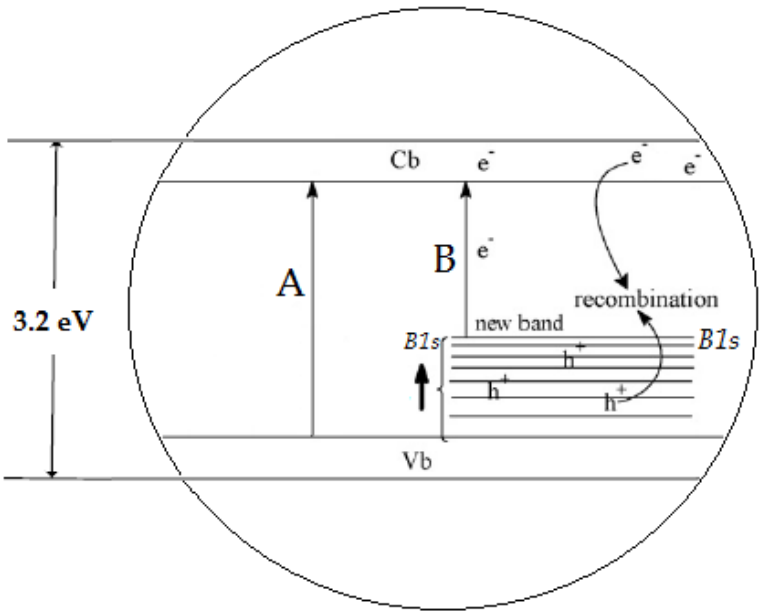

Figure 4.27. Schematic illustration of the photocatalysis mechanism for B-doped TiO_2 powder.

Further, UV-light photocatalytic oxidation reaction of MB by B-doped TiO_2 powders is described as followed. Since band gap energy is lowered in B-doped powders compared with as-received TiO_2 powder, energy of UV-light can generate more e^+-h^- couples resulting in higher photocatalytic activity.

$$B\text{-}TiO_2 + h\upsilon\ (UV) \longrightarrow e_{CB}^- + h_{VB}^+$$

The degradation of MB solution with time in dark and in UV illumination for reference TiO_2 powder and the Zr-doped TiO_2 powders is shown in Figure 4.28. The results of MB degradation occurred in these powders are presented in Table 4.13. It is obvious that all powders are active in the reaction of photocatalytic degradation of MB in UV illumination as well as in dark. When the powders were kept in dark for 30 min, milled TiO_2 powder decomposed only 46.7% of MB whereas $Zr_{0.5}$-TiO_2, $Zr_{1.0}$-TiO_2, and $Zr_{1.5}$-TiO_2 powders decomposed 49.2%, 48.1%, and 47.3% of MB, respectively. In dark, approximately 3% improvement in MB decomposition was achieved by 0.5% Zr doping. Further increase in Zr doping did not improve the photocatalytic efficiency of the Zr-doped TiO_2 powders. The improvement in MB decomposition as compared to milled TiO_2 powder was 2% and 1% of MB for $Zr_{1.0}$-TiO_2 and $Zr_{1.5}$-TiO_2 powders, respectively.

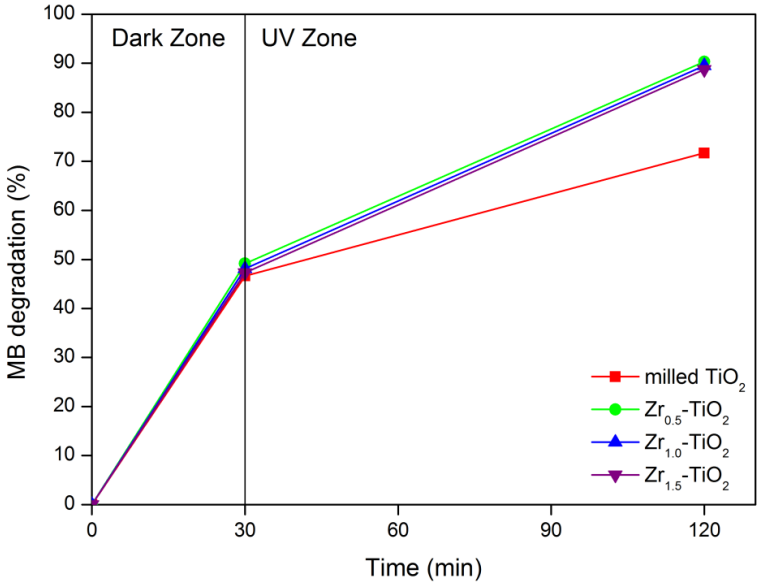

Figure 4.28. MB degradation with time in dark and in UV illumination for milled TiO_2 powder and the Zr-doped TiO_2 powders.

After exposing the powders to UV illumination for 90 min, total degradation of MB occurred for $Zr_{0.5}$-TiO_2, $Zr_{1.0}$-TiO_2, and $Zr_{1.5}$-TiO_2 powders were 90.3%, 89.5%, and 88.7%, respectively. It is clear that the MB degradation in UV illumination was more than that in dark for these powders, though the rate was lower. The MB degradation rate with time for these powders is separately shown in Figure 4.29.

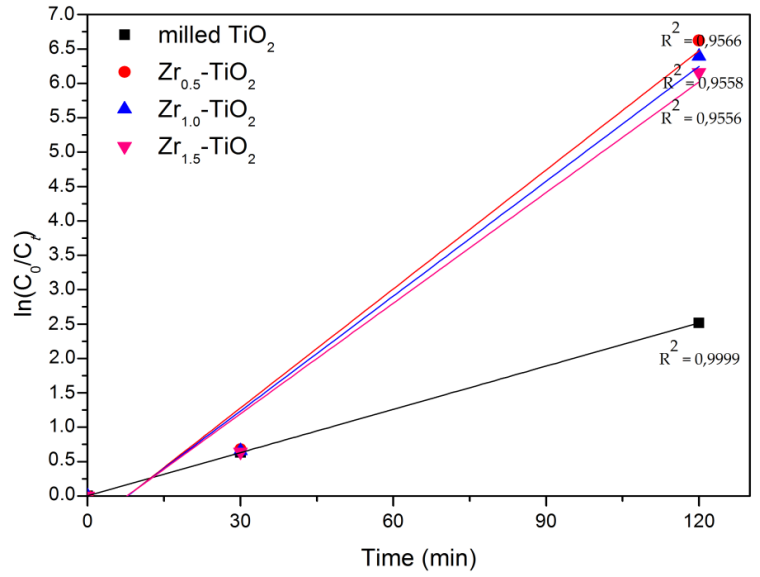

Figure 4.29. The variation of $\ln(C_0/C_t)$ with time for milled TiO_2 powder and the Zr-doped TiO_2 powders.

Small amount (0.5 wt%) of Zr doping improved the photocatalytic efficiency of milled TiO_2 powder. The MB degradation in UV illumination for $Zr_{0.5}$-TiO_2 powder (90.3%) was better than that for milled TiO_2 powder (71.7%) due to the narrowing of the band gap of TiO_2. The photocatalytic mechanism of Zr-doped TiO_2 powders is illustrated schematically in Figure 4.30. In the schematic illustration, photo generated electrons transferred from valence band to conduction band of undoped TiO_2 under UV illumination (process A). In Zr-doped TiO_2, substitution of Zr ions with Ti ions in TiO_2 lattice lowers the conduction band of TiO_2. Therefore, in Zr-doped TiO_2 powders, electrons can be excited simultaneously from valence band to Zr energy level (process B). Also, the photo generated electrons can easily transfer from the conduction band and the Zr doping energy level to the surface of photocatalyst to capture adsorbed O_2 which improves separation efficiency of charge carriers (Hoffmann et al., 1995). These two mechanisms give rise to increase in photocatalytic efficiency by ~17-19% in the Zr-doped powders as compared to undoped TiO_2 powder. Also, the adsorption of MB in dark depends on the interaction between π-electrons of MB ring and surface OH groups. Since there are many OH groups on the surface of TiO_2, oxidation states of Ti and O and thus, oxidation activity of TiO_2 powder could be increased by dopant Zr atoms which leads to improvement in adsorption capacity in the dark (Nguyen et al., 2012). Moreover, dopant Zr atoms in TiO_2 lattice restricts the recombination of electron-hole pairs at the surface of the photocatalyst thereby improves the visible light photocatalytic activity.

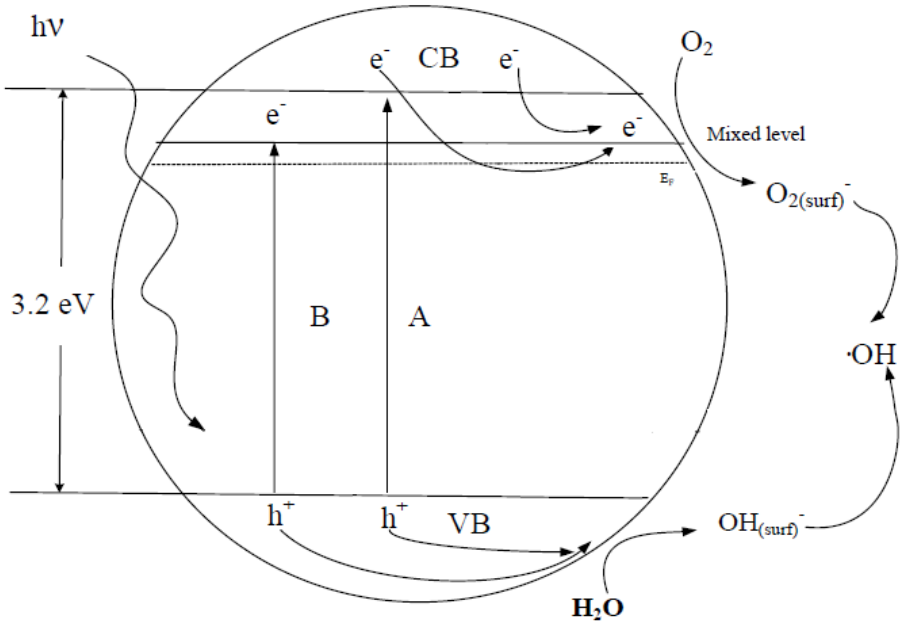

Figure 4.30. Schematic illustration of the photocatalysis mechanism for Zr-doped TiO_2 powder.

Further, UV-light photocatalytic oxidation reaction of MB by Zr-doped TiO_2 powders is described as followed. Since band gap energy is lowered in Zr-doped powders compared

with as-received TiO_2 powder, energy of UV-light can generate more e^+-h^- couples resulting in higher photocatalytic activity. Meanwhile, the photogenerated electrons (e_{CB}^-) can reduce Zr^{4+} species quickly and then, Zr^{3+} can be directly captured by the adsorbed O_2 molecules on the surface of TiO_2 and subsequently to form $\cdot O_2^-$ which can further react with the photogenerated electrons to reduce harmful pollutants.

$$Zr\text{-}TiO_2 + h\upsilon\ (UV) \longrightarrow e_{CB}^- + h_{VB}^+$$

$$Zr^{4+} + e_{CB}^- \longrightarrow Zr^{3+}$$

$$Zr^{3+} + O_2 \longrightarrow Zr^{4+} + \cdot O_2^-$$

Among the Zr-doped TiO_2 powders, $Zr_{0.5}$-TiO_2 powder offered the best individual photocatalytic efficiency in dark and in UV illumination. Further increase in Zr doping did not improve the photocatalytic efficiency of $Zr_{0.5}$-TiO_2 powder even in UV illumination. This is attributed to the amount of Zr ions present in the TiO_2 lattice. Rietveld analysis results in Section 4.1 revealed that more atomic sites of Zr in TiO_2 lattice were occupied in $Zr_{0.5}$-TiO_2 powder than $Zr_{1.0}$-TiO_2 and $Zr_{1.5}$-TiO_2 powders, implying that more Zr ions were incorporated into the TiO_2 lattice in $Zr_{0.5}$-TiO_2 powder. Therefore, the lowering effect of the conduction band was more active in $Zr_{0.5}$-TiO_2 powder than in $Zr_{1.0}$-TiO_2 and $Zr_{1.5}$-TiO_2 powders. Conclusively, 0.5 wt% of Zr doping was taken as the best amount of Zr concentration among the Zr-doped TiO_2 powders in terms of the improvement in the photocatalytic efficiency.

The degradation of MB solution with time in dark and in UV illumination for reference TiO_2 powder and the B-Zr co-doped TiO_2 powders is shown in Figure 4.31. The results of MB degradation occurred in these powders are presented in Table 4.17. It is obvious that all powders are active in the reaction of photocatalytic degradation of MB in UV illumination as well as in dark. When the powders were kept in the dark for 30 min, milled TiO_2 powder decomposed only 46.7% of MB whereas $B_{0.5}$-$Zr_{0.3}$-TiO_2, $B_{0.5}$-$Zr_{0.5}$-TiO_2, and $B_{0.5}$-$Zr_{0.7}$-TiO_2 powders decomposed 75.2%, 75.1%, and 74.6% of MB, respectively. In dark, approximately 30% improvement in MB adsorption was achieved by 0.5% B, and 0.3% Zr co-doping. Further increase in Zr doping did not improve the photocatalytic efficiency of the B-Zr co-doped TiO_2 powders. The improvement in MB decomposition as compared to milled TiO_2 powder was 30% and 29% of MB for $B_{0.5}$-$Zr_{0.5}$-TiO_2 and $B_{0.5}$-$Zr_{0.7}$-TiO_2 powders, respectively.

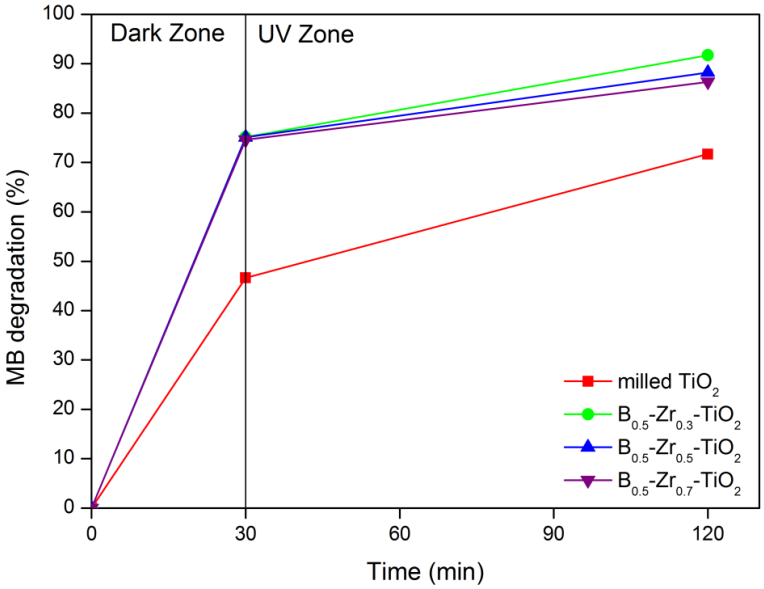

Figure 4.31. MB degradation with time in dark and in UV illumination for milled TiO_2 powder and the B-Zr co-doped TiO_2 powders.

After exposing the powders to UV illumination for 90 min, total degradation of MB occurred for $B_{0.5}$-$Zr_{0.3}$-TiO_2, $B_{0.5}$-$Zr_{0.5}$-TiO_2, and $B_{0.5}$-$Zr_{0.7}$-TiO_2 powders were 91.7%, 88.2%, and 86.3%, respectively. It is clear that the MB degradation in UV illumination was more than that in dark for these powders, though the rate was lower. The MB degradation rate with time for these powders is separately shown in Figure 4.32.

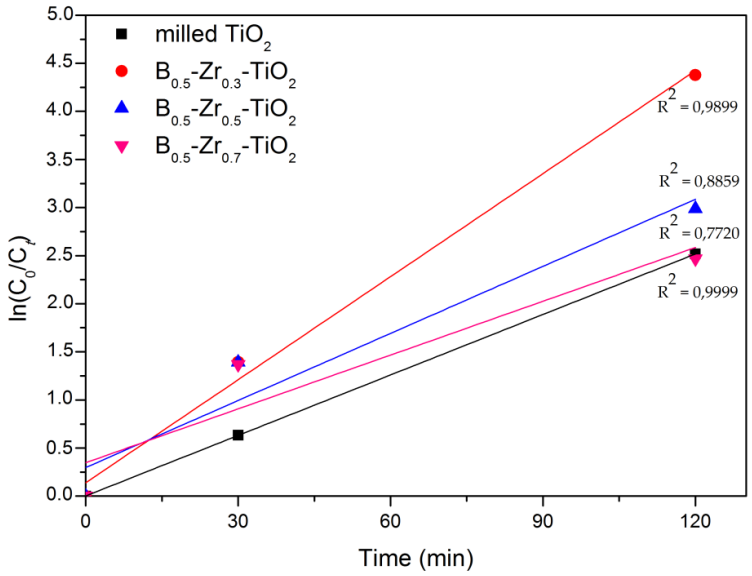

Figure 4.32. The variation of $\ln(C_0/C_t)$ with time for milled TiO_2 powder and the B-Zr co-doped TiO_2 powders.

The 0.5 wt% of B and 0.3 wt% of Zr co-doping improved the photocatalytic efficiency of milled TiO_2 powder. The MB degradation in UV illumination for $B_{0.5}$-$Zr_{0.3}$-TiO_2 powder (91.7%) was better than that for milled TiO_2 powder (71.7%) due to the narrowing of the band gap of TiO_2. The photocatalytic mechanism of B-Zr co-doped TiO_2 powders is illustrated schematically in Figure 4.33. In the schematic illustration, photo generated electrons transferred from valence band to conduction band of undoped TiO_2 under UV illumination (process A). Due to its wide band gap energy (3.2 eV), undoped TiO_2 showed relatively low photocatalytic efficiency for degradation of MB solution. After B doping, the interstitial B atoms in B-doped TiO_2 powders narrowed the band gap of TiO_2. Therefore, electrons can be excited simultaneously from the B1s energy level to conduction band (process C). After Zr doping, substitution of Zr ions with Ti ions in TiO_2 lattice lowers the conduction band of TiO_2. Therefore, electrons can be excited simultaneously from valence band to Zr energy level (process B). Also, the photo generated electrons can easily transfer from the conduction band and the Zr doping energy level to the surface of photocatalyst to capture adsorbed O_2 which improves separation efficiency of charge carriers. In B-Zr co-doped TiO_2, both processes B and C are active; thereby quantity of photo generated charge carriers could increase as compared to reference TiO_2, only B-doped TiO_2, and only Zr-doped TiO_2 powders. As a result, larger quantity of photo generated e^--h^+ pairs could participate in photodegradation process of MB resulting in higher photocatalytic performance of $B_{0.5}$-$Zr_{0.3}$-TiO_2 than that of undoped TiO_2, B-doped TiO_2, and Zr-doped TiO_2 powders. The combination of these two mechanisms give rise to increase in photocatalytic efficiency by ~30% in the B-Zr co-doped TiO_2 powders as compared to undoped TiO_2 powder. Also, the adsorption of MB in the dark depends on the interaction between π-electrons of MB ring and surface OH groups. Since there are many OH groups on the surface of TiO_2, oxidation states of Ti and O and thus, oxidation activity of TiO_2 powder could be increased by dopant B and Zr atoms which leads to improvement in adsorption capacity in the dark. Moreover, dopant Zr atoms in TiO_2 lattice restricts the recombination of electron-hole pairs at the surface of the photocatalyst thereby improves the visible light photocatalytic activity.

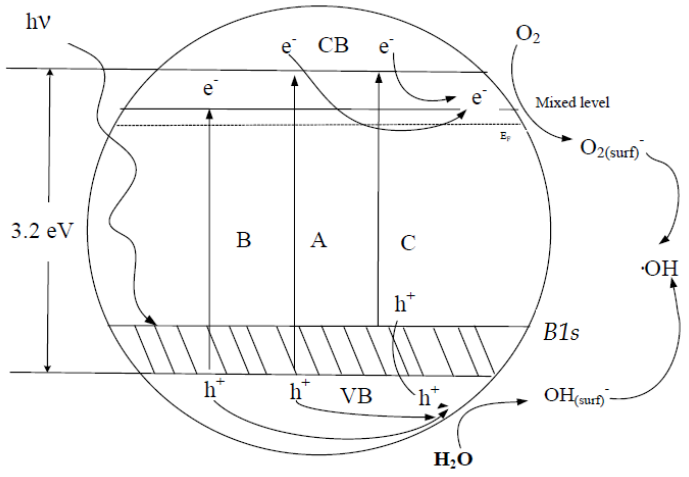

Figure 4.33. Schematic illustration of the photocatalysis mechanism for B-Zr co-doped TiO_2 powder.

Among the B-Zr co-doped TiO_2 powders, $B_{0.5}$-$Zr_{0.3}$-TiO_2 powder offered the best individual photocatalytic efficiency in dark and in UV illumination. Further increase in Zr doping did not improve the photocatalytic efficiency of $B_{0.5}$-$Zr_{0.3}$-TiO_2 powder even in UV illumination. This is attributed to the amount of Zr ions present in the TiO_2 lattice. Rietveld analysis results in Section 4.1 revealed that more atomic sites of Zr in TiO_2 lattice were occupied in $B_{0.5}$-$Zr_{0.3}$-TiO_2 powder than $B_{0.5}$-$Zr_{0.5}$-TiO_2 and $B_{0.5}$-$Zr_{0.7}$-TiO_2 powders, implying that more Zr ions were incorporated into the TiO_2 lattice in $B_{0.5}$-$Zr_{0.3}$-TiO_2 powder. Therefore, the lowering effect of the conduction band was more active in $B_{0.5}$-$Zr_{0.3}$-TiO_2 powder than in $B_{0.5}$-$Zr_{0.5}$-TiO_2 and $B_{0.5}$-$Zr_{0.7}$-TiO_2 powders. Conclusively, 0.5 wt% of B and 0.3 wt% of Zr co-doping was taken as the best amount of B and Zr concentrations among the B-Zr co-doped TiO_2 powders in terms of the improvement in the photocatalytic efficiency.

Further, photocatalytic oxidation process of MB is described as followed. Reactions (1)-(7) describe TiO_2 activation mechanism by UV irradiation (Konstantinou and Albanis, 2004). Firstly, conduction band electrons (e^-) and valance band holes (h^+) are generated from aqueous TiO_2 suspension by UV irradiation (1).

$$B\text{-}Zr\text{-}TiO_2 + h\upsilon\ (UV) \longrightarrow e_{CB^-} + h_{VB^+} \quad (1)$$

Meanwhile, the photogenerated electrons (e_{CB^-}) can reduce Zr^{4+} species quickly (2) and then, Zr^{3+} can be directly captured by the adsorbed O_2 molecules on the surface of TiO_2(3). Also, the photogenerated electrons (e_{CB^-}) can reduce the adsorbed O_2 molecules on the surface of TiO_2 (4) subsequently to form hydrogen peroxide (H_2O_2) (5), which can further react with photogenerated electrons to produce active ·OH radicals (6).

$$Zr^{4+} + e_{CB^-} \longrightarrow Zr^{3+} \quad (2)$$

$$Zr^{3+} + O_2 \longrightarrow Zr^{4+} + \cdot O_2^- \quad (3)$$

$$TiO_2(e_{CB^-}) + O_2 \longrightarrow TiO_2 + \cdot O_2^- \quad (4)$$

$$\cdot O_2^- + e_{CB^-} + 2H^+ \longrightarrow H_2O_2 \quad (5)$$

$$H_2O_2 + e_{CB^-} \longrightarrow \cdot OH + OH^- \quad (6)$$

Meanwhile, the photogenerated holes (h_{VB^+}) can react with OH^- (7) or H_2O (8) oxidizing them into ·OH radicals which were known to be the most oxidizing species (standart redox potential +2.8 V). Eventually, MB molecules were mineralized into small molecules, such as CO_2, H_2O at the TiO_2 surface (9).

$$TiO_2(h_{VB^+}) + OH^- \longrightarrow TiO_2 + \cdot OH \quad (7)$$

$$TiO_2(h_{VB^+}) + H_2O \longrightarrow TiO_2 + H^+ + \cdot OH \quad (8)$$

$$MB + \cdot OH \longrightarrow \text{degradation products} \quad (9)$$

The total degradation of MB solution in UV illumination for all of the powders investigated was compared with each other in Figure 4.34.

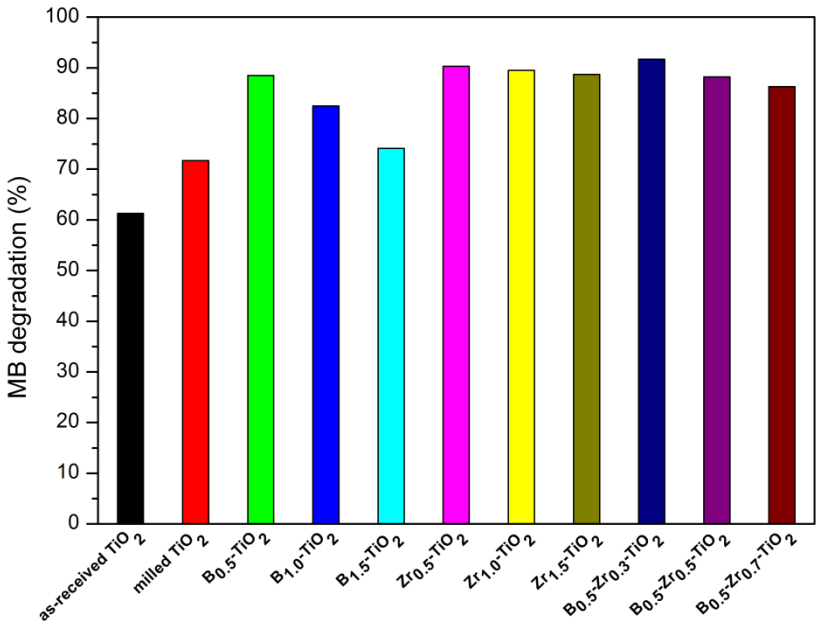

Figure 4.34. Total MB degradation in UV illumination for all of the powders investigated.

Among all of the powders investigated, the best photocatalytic efficiency was assigned to $B_{0.5}$-$Zr_{0.3}$-TiO_2 powder, for which 91.7% of MB solution degraded after 30 min in dark followed by 2 h UV-illumination. The photocatalytic efficiency of $B_{0.5}$-$Zr_{0.3}$-TiO_2 powder was approximately 20% better than that of the reference powder. The results revealed that cooperative effect of B and Zr doping was outstanding in terms of photocatalytic efficiency. The higher photocatalytic activity of $B_{0.5}$-$Zr_{0.3}$-TiO_2 powder is linked to the high anatase crystallinity, large specific surface area, intense light absorption, adsorption capacity in dark, and narrower band gap energy. Furthermore, better photocatalytic efficiency of the powders in the order $B_{0.5}$-$Zr_{0.3}$-TiO_2 > $Zr_{0.5}$-TiO_2 > $B_{0.5}$-TiO_2 was consistent with the increase in cell volumes 136.87 $Å^3$ > 136.60 $Å^3$ > 136.48 $Å^3$ obtained from Rietveld analysis in section 4.2.1. Consequently, extent of distortion in TiO_2 crystal lattice is directly related to photocatalytic efficiency.

CHAPTER 5

CONCLUSIONS

An investigation of the photocatalytic properties of B-Zr co-doped TiO_2 powders prepared by mechanical ball milling has led to the following conclusions.

1. The B-Zr co-doped photocatalyst TiO_2 could be successfully prepared by mechanical ball milling.
2. Conventional ball milling process used for the photocatalyst preparation gives rise to better surface properties and photocatalytic activity of TiO_2 powders.
3. B atoms could be doped interstitially whereas Zr atoms could be doped substitutionally into the crystal lattice of TiO_2.
4. B doping as well as Zr doping into TiO_2 lattice cause some degree of distortion and increases the cell volume of TiO_2.
5. B-Zr co-doping provides the highest distortion in TiO_2 lattice and extent of distortion is directly related to photocatalytic efficiency.
6. The photocatalytic degradation rate of MB solution could be greatly improved by B and/or Zr doping into TiO_2 lattice.
7. Compared with as-received TiO_2 powder, B-Zr co-doped TiO_2 powder exhibits a 10% enhancement in photocatalytic efficiency for the degradation of MB solution in UV- illumination.
8. Synergistic effects of B-Zr co-doping and particle size reduction are responsible for improvement in the photocatalytic efficiency.

REFERENCES

- Almquist, C. B., & Biswas, P. (2002). Role of synthesis method and particle size of nanostructured TiO_2 on its photoactivity. *Journal of Catalysis, 212*, 145-156.
- Al-Ghouti, M. A., Khraisheh, M. A. M., Ahmad, M. N. M., & Allen S. (2009). Adsorption behaviour of methylene blue on Jordanian diatomite: A kinetic study. *Journal of Hazardous Materials, 165*, 589-598.
- Bacsa, R. R., & Gratzel, M. (1996). Rutile formation in hydrothermally crystallized nanosized titania. *Journal of American Ceramic Society, 79*, 2185.
- Bao, X. W., Yan S. S., Chen, F., & Zhang J. I. (2005). Preparation of TiO_2 photocatalyst by hydrothermal method from aqueous peroxotitanium acid gel. *Materials Letters, 59*, 412-415.
- Bastl, Z., Senkevich, A. I., Spirova, I., & Vrtilkova, V. (2002). Angle-resolved core-level spectroscopy of Zr1Nb alloy oxidation by oxygen, water and hydrogen peroxide. *Surface and Interface Analysis, 34*, 477-480.
- Bryne, J. A., Fernandez-Ibanez, P. A., Dunlop, P. S. M., Alrousan, D. M. A., & Hamilton, J. W. J. (2011). Photocatalytic enhancement for solar disinfection of water: A Review. *International Journal of Photoenergy, 2011*, 1-12.
- Carp, O., Huisman, C. L., & Reller, A. (2004). Photoinduced reactivity of titanium dioxide. *Progress in Solid State Chemistry, 32*, 33-177.
- Cernea, M., Valsangiacom, C., Trusca, R., & Vasiliu, F. (2007). Synthesis of iron-doped anatase-TiO_2 powders by a particulate sol-gel route. *Journal of Optoelectronics and Advanced Materials, 9*, 2648-2652
- Chatterjee, D., & Dasgupta, S. (2005). Visible light induced photocatalytic degradation of organic pollutants. *Journal of Photochemistry and Photobiology C: Photochemistry Reviews, 6*, 186-205.
- Chen, D., Yang, D., Wang, Q., & Jiang, Z. (2006). Effects of boron doping on photocatalytic activity and microstructure of titanium dioxide nanoparticles. *Industrial & Engineering Chemistry Research, 45*, 4110-4116.
- Cheng, X., Yu, X., & Xing, Z. (2012). One-step synthesis of visible active C-N-S tridoped TiO_2 photocatalyst from biomolecule cystine. *Applied Surface Science, 258*, 7644-7650.
- Choi, W. S., Chung, H. Y., Yoon, B. R., & Kim, S. S. (2001). Application of grinding kinetic analysis to fine grinding characteristics of some inorganic materials using a composite grinding media by planetary ball mill. *Powder Technology, 115*, 209-214.
- Colon, G., Maicu, M., Hidalgo, M. C., & Navio J. A. (2006). Cu-doped TiO_2 systems with improved photocatalytic activity. *Applied Catalysis B: Environmental, 67*, 41-51.
- Dutta, H., Sahu, P., Pradhan, S. K., & De, M. (2002). Microstructure characterization of polymorphic transformed ball-milled anatase TiO_2 by Rietveld method. *Materials Chemistry and Physics, 77*, 153-164.
- Ersöz, İ. T. (2009). *Application of semiconductor films over glass/ceramic surfaces and their low temperature photocatalytic activity*. Master's thesis, Middle East Technical University, Ankara, Turkey.
- Fahmi, A., Minot, C., Silvi, B., & Causa, M. (1993). Theoretical analysis of the structures of titanium dioxide crystals. *Physical Review B, 47*, 11717-11724.

- Fan, L., Dongmei, J., & Xueming, M. (2009). The effect of milling atmospheres on photocatalytic property of Fe-doped TiO_2 synthesized by mechanical alloying. *Journal of Alloys and Compounds, 470*, 375-378.
- Fujishima, A., Rao, T. N., & Tryk, D. A. (2000). Titanium dioxide photocatalysis. *Journal of Photochemistry and Photobiology C: Photochemistry reviews, 1*, 1-21.
- Fujishima, A., Zhang, X., & Tryk, D. A. (2007). Heterogeneous photocatalysis: From water photolysis to applications in environmental cleanup. *International Journal of Hydrogen Energy, 32*, 2664-2672.
- Gao, B., Lim, T. M., Subagio, D. P., & Lim, T. T. (2010). Zr-doped TiO_2 for enhanced photocatalytic degradation of bisphenol A. *Applied Catalysis A: General, 375*, 107-115.
- Geng, H., Yin, S., Yang, X., Shuai, Z., & Liu, B. (2006). Geometric and electronic structure of the boron-doped photocatalyst TiO_2. *Journal of Physics: Condensed Matter, 18*, 87-96.
- Hahn, T. (2005). *International Tables for Crystallography Volume A: Space-Group Symmetry, 5th Ed.*, The International Union of Crystallography, Chester, England.
- Han, J. J., Kim, D. H., Kim, S. J., & Lee, K. S. (2008). Synthesis and photocatalytic property of a mixture of anatase and rutile TiO_2 doped with Fe by mechanical alloying process. *Journal of Alloys and Compounds, 459*, 386-389.
- Hennart, S. L. A., Hee, P. V., Drouet, V., Domingues, M. C., Wildeboer, W. J., & Meesters, G. M. H. (2012). Characterization and modelling of sub-micron milling process limited by agglomeration phenomena. *Chemical Engineering Science, 71*, 484-495.
- Hernandez-Alonso, M. D., Fresno, F., Suarez, S., & Coronado, M. J. (2009). Development of alternative photocatalysts to TiO_2: Challenges and opportunities, *Energy & Environmental Science*, *2*, 1231-1257.
- Ho, W., Yu, J. C., & Lee, S. (2006). Synthesis of hierarchical nanoporous F-doped TiO_2 spheres with visible light photocatalytic activity. *Chemical Community, 1115*, 1115-1117.
- Hoffmann, M. R., Martin, S. T., Choi, W., & Bahnemannt, D. W. (1995). Environmental Applications of Semiconductor Photocatalysis. *Chemical Reviews, 95*, 69-96.
- Hong, Y. C., Bang, C. U., Shin, D. H., & Uhm, H. S. (2005). Band gap narrowing of TiO_2 by nitrogen doping in atmospheric microwave plasma. *Chemical Physics Letters, 413*, 454-457.
- Ishibai, Y., Sato, J., Akita, S., Nishikawa, T., & Miyagishi, S. (2007). Photocatalytic oxidation of NO_x by Pt-modified TiO_2 under visible illumination. *Journal of Photochemistry and Photobiology A: Chemistry, 188*, 106-1111.
- Jang, H. D., Kim, S. K., & Kim, S. J. (2001). Effect of particle size and phase composition of titanium dioxide nanoparticles on the photocatalytic properties. *Journal of Nanoparticle Research, 3*, 141-147.
- Joyner, D. J., & Hercules, D. M. (1980). Chemical bonding and electronic structure of B_2O_3, H_3BO_3, and BN: An ESCA, Auger, SIMS, and SXS study. *Journal of Chemical Physics, 72*, 1095-1109.
- Jung, K. Y., Park, S. B., & Ihm, S. K. (2004). Local structure and photocatalytic activity of B_2O_3-SiO_2/TiO_2 ternary mixed oxides prepared by sol-gel method. *Applied Catalysis B: Environmental, 51*, 239-245.

- Kang, I. C., Zhang, Q., Yin, S., Sato, T., & Saito, F. (2008). Preparation of a visible sensitive carbon doped TiO_2 photo-catalyst by grinding TiO_2 with ethanol and heating treatment. *Applied Catalysis B: Environmental, 80*, 81-87.
- Khan, R., Kim, S. W., Kim, T. J., & Nam, C. M. (2008). Comparative study of the photocatalytic performance of boron-iron co-doped and boron-doped TiO_2 nanoparticles. *Materials Chemistry and Physics, 112*, 167-172.
- Kolen'ko, Y. V., Maximov, V. D., Garshev, A. V., Meskin, P. E., Oleynikov, N. N., & Churagulov, B. R. (2004). Hydrothermal synthesis of nanocrystalline and mesoporous titania from aqueous complex titanyl oxalate acid solution. *Chemical Physics Letters, 388*, 411-415.
- Kumerasan, L., Prabhu, A., Palanichamy, M., Arumuguam, E., & Murugesan, V. (2011). Synthesis and characterization of Zr^{4+}, La^{3+}, and Ce^{3+} doped mesoporous TiO_2: Evaluation of their photocatalytic activity. *Journal of Hazardous Materials, 186*, 1183-1192.
- Konstantinou, I. K., & Albanis, T. A. (2004). TiO_2-assisted photocatalytic degradation of azo dyes in aqueous solution: kinetic and mechanistic investigations. A review. *Applied Catalysis B: Environmental, 49*, 1-14.
- Larson, A. C., & Von Dreele, R. B. (2004). *General Structure Analysis System (GSAS)*. The Regents of the University of California, California, United States.
- Lee, S., Cho, I. S., Noh, J. H., Hong, K. S., Han, G. S., Jung, H. S., Jeong, S., Lee, C., & Shin, H. (2010). *Physica Status Solidi A, 207*, 2288-2291.
- Legrini, O., Oliveros, E., & Braun, A. M. (1993). Photochemical process for water treatment. *Chemical Reviews, 93*, 671-698.
- Li, F., & Liu, T. (2011). Method for producing high-active titanium dioxide hydrosol by using metatitanate as precursor. *Unites States Patent*, US 7,897,137 B2.
- Li, H., Li, J., & Huo, Y. (2006). Highly active TiO_2N photocatalysts prepared by treating TiO_2 precursors in NH_3/Ethanol fluid under supercritical conditions. *Journal of Physical Chemistry B, 110*, 1559-1565.
- Lin, L., Lin, W., Xie, J. L., Zhu, Y. X., Zhao, B. Y., & Xie, Y. C. (2007). Photocatalytic properties of phosphor-doped titania nanoparticles. *Applied Catalysis B: Environmental, 75*, 52-58.
- Ling, Q., Sun, J., Zhou, Q., Ren, H., & Zhao, Q. (2008). Visible-light-driven titania/silica photocatalyst co-doped with boron and ferrum. Applied Surface Science, 254, 6731-6735.
- Linsebigler, A. L., Lu, G., & Yates, J. T. (1995). Photocatalysis on TiO_2 surfaces: Principles, mechanisms, and selected results. *Chemcial Reviews, 95(3)*, 735-758.
- Liu, B., Wen, L., Nakata, K., Zhao, X., Liu, S., Ochiai, T., Murakami, T., & Fujishima, A. (2012). Polymeric adsorption of methylene blue in TiO_2 colloids-Highly sensitive thermochromism and selective photocatalysis. *Chemistry A European Journal, 18*, 12705-12711.
- Liu, J. W., Han, R., Wang, H. T., Zhao, Y., Lu, W. J., Wu, H. Y., Yu, T. F., & Zhang, Y. X. (2011). Degradation of PCP-Na with La-B co-doped TiO_2 series synthesized by the sol-gel hydrothermal method under visible and solar illumination. *Journal of Molecular Catalysis A: Chemical, 344*, 145-152.
- Maira, A. J., Yeung, K. L., Lee, C. Y., Yue P. L., & Chan C. K. (2000). Size effects in gas-phase photo-oxidation of trichloroethylene using nanometer-sized TiO_2 catalysts. *Journal of Catalysis, 192*, 185-196.

- Manik, S. K., Bose, P., & Pradhan, S. K. (2003). Microstructure characterization and phase transformation kinetics of ball-milled prepared nanocrystalline Zn_2TiO_4 by Rietveld method. *Materials Chemistry and Physics, 82*, 837-847.
- Maurya, A., & Chauhan, P. (2011). Structural and optical characterization of CdS/TiO_2 nanocomposite. *Materials Characterization, 62*, 382-390.
- Mavel, G., Escard, J., Costa, P., & Castaing, J. (1973). ESCA surface study of metal borides. *Surface Science, 35*, 109-116.
- Mills, A., & Hunte, S. L. (1997). An overview of semiconductor photocatalysis. *Journal of Photochemistry and Photobiology A: Chemistry, 108*, 1-35.
- Moellmann, J., Ehrlich, S., Tonner, R., & Grimme, S. A DFT-D study of structural and energetic properties of TiO_2 modifications. Journal of Physics: Condensed Matter, 24, 424206-424215.
- Nakata, K., & Fujishima, A. (2012). TiO_2 photocatalysis: Design and applications. *Journal of Photochemistry and Photobiology C: Photochemistry Reviews, 13*, 169-189.
- Nakata, K., Ochiai, T., Murakami, T., & Fujishima, A. (2012). Photoenergy conversion with TiO_2 photocatalysis: New materials and recent applications. *Electrochimica Acta, 84*, 103-111.
- Nam, W. S., & Han, G. Y. (2003). A photocatalytic performance of TiO_2 photocatalyst prepared by hydrothermal method. *Korean Journal of Chemical Engineering, 20(1)*, 180-184.
- Nguyen, T. B., Hwang, M. J., & Ryu, K. S. (2012). High adsorption capacity of V-doped TiO_2 for decolorization of methylene blue. *Applied Surface Science, 258*, 7299-7305.
- Nguyen-Phan, T. D., Song, M. B., Yun, H., Kim, E. J., Oh, E. S., Shin, & E. W. (2011). Characterization of vanadium-doped mesoporous titania and its adsorption of gaseous benzene. *Applied Surface Science, 257*, 2024-2031.
- Niederberger, M., & Pinna, N. (2009). Aqueous and nonaqueous sol-gel. In *Metal Oxide Nanoparticles in Organic Solvents: Synthesis, Formation, Assembly and Application* (pp. 7-17).
- Ohno, T., Akiyoshi, M., Umebayashi, T., Asai, K., Mitsui, T., & Matsumura, M. (2004). Preparation of S-doped TiO2 photocatalysts and their photocatalytic activities under visible light. *Applied Catalysis A: General, 265*, 115-121.
- Ohtani, B., & Nishimoto, S. (1993). Effect of surface adsorptions of aliphatic alcohols and silver ion on the photocatalytic activity of titania suspended in aqueous solutions. *The Journal of Physical Chemistry, 97(4)*, 920-926.
- Park, J. (2010). Photocatalytic activity of hydroxyapatite-precipitated potassium titanate whiskers. *Journal of Alloys and Compounds, 492*, L57-L60.
- Park, H. S., Kim, D. H., Kim, S. J., & Lee, K. S. (2006). The photocatalytic activity of 2.5 wt% Cu-doped TiO_2 nano powders synthesized by mechanical alloying. *Journal of Alloys and Compounds, 415*, 51-55.
- Parrino, F., Augugliaro, V., Camera-Roda, G., Loddo, V., Lopez-Munoz, M. J., Marquez-Alvarez, C., Palmisano, G., Palmisano, L., & Puma, M. A. (2012). Visible-light-induced oxidation of trans-ferulic acid by TiO_2 photocatalysis. *Journal of Catalysis, 294*, 254-260.
- Pham, T. H., & Brindley, G.W. (1970). Metyhlene blue absorption by clay minerals. Determination of surface areas and cation exchange capacities. *Clays and Clay Minerals, 18*, 203-212.

- Reddy, B. M., Bharali, P., Saikia, P., Thrimurthulu, G., Yamada, Y., & Kobayashi, T. (2009). Thermal stability and dispersion behavior of nanostructured $Ce_xZr_{1-x}O_2$ mixed oxide over anatase-TiO_2: A combined study of CO oxidation and characterization by XRD, XPS, TPR, HREM, and UV-Vis DRS. *Industrial & Engineering Chemistry Research, 48*, 453-462.
- Rouquérol, F., Rouquéerol, J., & Sing, K. S. W. (1999). Adsorption by Powders & Porous Solids: Principles, Methodology and Applications, Academic Press, 157-161.
- Sakatani, Y., Nunoshige, J., Ando, H., Okusako, K., Koike, H., Takata, T., Kondo, J. N., Hara, M., & Domen, K. (2003). Photocatalytic decomposition of acetaldehyde under visible illumination over La^{3+} and N co-doped TiO_2. *Chemistry Letters, 32*, 1156-1157.
- Salah, N., Habib, S. S., Khan, Z. H., Memic, A., Azam, A., Alarfaj, E., Zahed, N., & Al-Hamedi, S. (2011). High-energy ball milling technique for ZnO nanoparticles as antibacterial material. *International Journal of Nanomedicine, 6*, 863-869.
- Schreifels, J., Maybury, P., & Swartz, W. J. (1980). X-ray photoelectron spectroscopy of nickel boride catalysts: Correlation of surface states with reaction products in the hydrogenation of acrylonitrile. *Journal of Catalysis, 65*, 195-206.
- Shifu, C., Wei, Z., Wei, L., & Sujuan, Z. (2008) Preparation, characterization and activity evaluation of p-n junction photocatalyst p-ZnO/n-TiO_2. *Applied Surface Science, 255*, 2478- 2484.
- Sobana, N., Muruganadham, M., & Swaminathan, M. (2006) Nano-Ag particles doped TiO_2 for efficient photodegradation of direct azo dyes. *Journal of Molecular Catalysis A: Chemical, 258*, 124-132.
- Stamate, M., & Lazar, G. (2007). Application of titanium dioxide photocatalysis to create self-cleaning materials. *Romanian Technical Sciences Academy, 3*, 280-285.
- Su, C., Hong, B., & Tseng, C. (2004). Sol-gel preparation and photocatalysis of titanium dioxide. *Catalysis Today, 96*, 119-126.
- Sun, J., Gao, L., & Zhang, Q. (2003). Synthesizing and comparing the photocatalytic properties of high surface area rutile and anatase titania nanoparticles. *Journal of American Ceramic Society, 86*, 1677-1682.
- Suryanarayana, C. (2001). Mechanical alloying and milling. *Progress in Materials Science, 46*, 1-184.
- Tian, H., Ma, J., Li, K., & Li, J. (2008). Photocatalytic degradation of methyl orange with W-doped TiO_2 synthesized by a hydrothermal method. *Materials Chemistry and Physics, 112*, 47-51.
- Toby, B. H. (2001). EXPGUI, a graphical user interface for GSAS. *Journal of Applied Crystallography, 34*, 210-213.
- Uhm, Y. R., Woo, S. H., Kim, W. W., Kim, S. J., & Rhee, C. K. (2006). The characterization of magnetic and photo-catalytic properties of nanocrystalline Ni-doped TiO_2 powder synthesized by mechanical alloying. *Journal of Magnetism and Magnetic Materials, 304*, 781-783.
- Venkatachalam, N., Palanichamy, M., Arabindoo, B., & Murugesan, V. (2007). *Journal of Molecular Photocatalysis A: Chemical, 266*, 158-165.
- Wei, C. H., Tang, X. H., Liang, J. R., & Tan, S. Y. (2007). Preparation, characterization and photocatalytic activities of boron-and cerium-codoped TiO_2. *Journal of Environmental Sciences, 19*, 90-96.

- Weirich, T. E., Winterer, M., Seifried, S., Hahn, H., & Fuess, H. (2000). Rietveld analysis of electron powder diffraction data from nanocrystalline anatase, TiO_2. *Ultramicroscopy, 81*, 263-270.
- Winburn, R. S. (2003). Rietveld analysis of complex mixtures. What can we do? *Advances in X-ray Analysis, 46*, 210-219.
- Woo, S. H., Kim, W. W., Kim, S. J., & Rhee, C. K. (2007). Photocatalytic behaviors of transition metal ion doped TiO_2 powder synthesized by mechanical alloying. *Materials Science and Engineering: A, 449-451*, 1151-1154.
- Xie, J., Lü, X., Liu, J., & Shu, H. (2009). Brookite titania photocatalytic nanomaterials: Synthesis, properties, and applications. *Pure and Applied Chemistry, 81(12)*, 2407-2415.
- Xu, N., Shi, Z., Fan, Y., Dong, J., Shi, J., & Hu, M. Z. C. (1999). Effects of particle size of TiO_2 on photocatalytic degradation of methylene blue in aqueous suspensions. *Industrial & Engineering Chemistry Research, 38*, 373-379.
- Yao, X., Wang, X., Su, L., Yan, H., & Yao, M. (2011). Band structure and photocatalytic properties of N/Zr co-doped anatase TiO_2 from first-principles study. *Journal of Molecular Catalysis A: Chemical, 351*, 11-16.
- Yuan, J., Wang, E., Chen, Y., Yang, W., Yao, J., & Cao, Y. (2011). Doping mode, band structure and photocatalytic mechanism of B-N-codoped TiO_2. *Applied Surface Science, 257*, 7335-7342.
- Zhang, X., & Liu, Q. (2008). Preparation and characterization of titania photocatalyst co-doped with boron, nickel, and cerium. *Materials Letters, 62*, 2589-2592.
- Zhang, X., & Liu, Q. (2008). Visible-light-induced degradation of formaldehyde over titania photocatalyst co-doped with nitrogen and nickel. *Applied Surface Science, 254*, 4780-4785.
- Zhang, Z., Wang, C. C., Zakaria, R., & Ying J. Y. (1998). Role of particle size in nanocrystalline TiO_2-based photocatalysts. *The Journal of Physical Chemistry B, 102*, 10871-10878.
- Zhao, J., & Yang, X. (2003). Photocatalytic oxidation for indoor air purification: a literature review. *Building and Environment, 38*, 645-654.
- Zhu, J., Zheng, W., He, B., Zhang, J., & Anpo, M. (2004). Characterization of Fe-TiO_2 photocatalysts synthesized by hydrothermal method and their photocatalytic reactivity for photodegradation of XRG dye diluted in water. *Journal of Molecular Catalysis A: Chemical, 216*, 35-43.